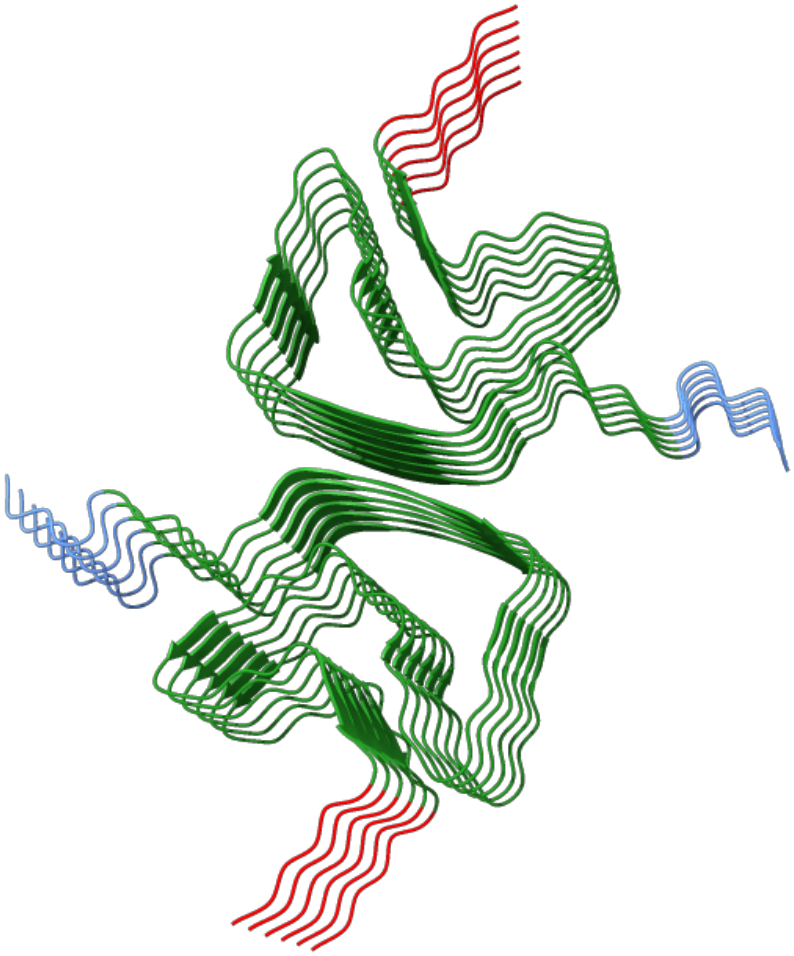

Catalytic Activity of Amyloids of α-Synuclein Variants with Pathological Mutations

Master's thesis in Biomedical Engineering

AMAR EL ISSAOUI

DEPARTMENT OF LIFE SCIENCES
CHALMERS UNIVERSITY OF TECHNOLOGY
Gothenburg, Sweden 2025
www.chalmers.se

Master's thesis 2025

Catalytic Activity of Amyloids of α-Synuclein Variants with Pathological Mutations

AMAR EL ISSAOUI

CHALMERS
UNIVERSITY OF TECHNOLOGY

Department of Life Sciences
Division of Chemical Biology
Wittung-Stafshede Protein Biophysics Lab
Chalmers University of Technology
Gothenburg, Sweden 2025

Catalytic Activity of Amyloids of α-Synuclein Variants with Pathological Mutations
AMAR EL ISSAOUI

Supervisor: István Horvath, Life Sciences
Examiner: Pernilla Wittung-Stafshede, Life Sciences

Master's Thesis 2025
Department of Life Sciences
Division of Chemical Biology
Wittung-Stafshede's Protein Biophysics lab
Chalmers University of Technology
SE-412 96 Gothenburg
Telephone +46 31 772 1000

Cover: Structure of wild-type α-Synuclein fibrils determined by cryo-EM (PDB ID: 6A6B). Image was rendered using UCSF Chimera.

Typeset in LaTeX
Printed by Chalmers Reproservice
Gothenburg, Sweden 2025

Catalytic Activity of Amyloids of α-Synuclein Variants with Pathological Mutations
AMAR EL ISSAOUI
Department of Life Sciences
Chalmers University of Technology

Abstract

Parkinson's disease is a progressive neurogenerative disorder which is characterized by the presence of Lewy bodies, which consist of insoluble α-Synuclein amyloid aggregates. While amyloids have been considered to be inert end-products, recent studies show that some amyloids exhibit catalytic properties. This master's thesis focuses on the catalytic activity of α-Synuclein, including the wild-type and three pathological mutations: E46K, H50Q and A53T. In this thesis, the monomers of each variant were over-expressed in Escherichia coli, purified, aggregated as well as quality controlled through circular dichroism, Thioflavin T fluorescence and atomic force microscopy. The catalytic activity of these four amyloid fibril variants were studied in relation of their control group consisting either monomers or buffer background. Substrate paranitrophenyl acetate was used to study esterase activity, while paranitrophenyl phosphate and adenosine 5'-triphosphate were used for dephosphorylation assays. Results show that all variants exhibit strong esterase activity, while phosphatase activity varies between the variants and individual experiments, suggesting sensitivity on how amyloid fibrils are prepared. The dephosphorylation results are discussed in terms of how fibril polymorphism may influences the catalytic activity. While esterase activity was high, the differences between the variants were not statistically significant enough to draw firm conclusions.

Keywords: Alpha-Synuclein, amyloid fibrils, catalytic activity, Parkinson's disease, pathological mutations.

Acknowledgements

I would like to thank my examiner Professor Pernilla Wittung-Stafshede for overseeing the project, for her insightful advice that sharpened this thesis and for all the opportunities during this project, including the ADAM10 conference. I would like to thank my supervisor Istvan Horváth for his continuous guidance and helping me to get started with everything in the laboratory work and answering all my questions. I also thank Ranjeet Kumar for preparing most of the proteins used in this thesis. I am very grateful for all the members in the Wittung-Stafshede group for their support and the Division of Chemical Biology for practical help and good spirits whenever needed. Above all, I thank my family and friends for their encouragement and unconditional support throughout the completion of this project.

Amar el Issaoui, Gothenburg, June 2025

List of Acronyms

Below is the list of acronyms that have been used throughout this thesis listed in alphabetical order:

A53T	Alanine-53-Threonine
AFM	Atomic force microscopy
aSyn	α-Synuclein
ATP	Adenosine 5'-triphosphate
CD	Circular dichroism
E46K	Glutamate-46-Lysine
H50Q	Histidine-50-Glutamine
MM	Michaelis-Menten
MW	Molecular weight
PD	Parkinson's disease
pNP	Paranitrophenol
pNPA	Paranitrophenyl acetate
pNPP	Paranitrophenyl phosphate
SD	Standard deviation
SDS-PAGE	Sodium dodecyl sulfate polyacrylamide gel electrophoresis
SEC	Size-exclusion chromatography
ThT	Thioflavin T
WT	Wild-type

Contents

List of Figures

List of Tables

1
Introduction

Neurodegenerative diseases are rising in the aging population, increasing a burden on individuals and healthcare systems worldwide [1]. Among these disorders, Alzheimer's Disease (AD) and Parkinson's Disease (PD) stand out as the two most common neurodegenerative diseases associated with the pathological accumulation of amyloid fibrils [1], [2]. These diseases normally arise when soluble protein monomers misfold and self-assemble into insoluble, cross-β–rich fibrils [3]. In PD, these fibrils are composed primarily of α-synuclein (aSyn) and accumulate as Lewy bodies inside the neuronal cells [4]. The presence of these bodies defines the main hallmark of PD.

Although amyloid fibrils have been considered inert "dead-end" aggregates, recent studies have showed that these fibrils are able to catalyze chemical reactions in vitro [5]. For example, glucagon and Aβ fibrils from AD have been shown to promote ester and peptide bond hydrolysis, and wild-type (WT) aSyn fibrils catalyze both esterase and dephosphorylation reactions [5], [6]. These activities are absent in their monomeric forms. Another study confirms altered metabolite levels in neuronal cells when incubated with aSyn fibrils, suggesting that the enzymatic activity of aSyn fibrils may disrupt normal cellular metabolism [7].

Familial mutations in SNCA gene highlights how subtle changes in primary sequence can influence both amyloid formation and disease onset [8]. Variants such as A30P, E46K, and A53T are associated with early-onset PD, whereas H50Q and the WT sequence are more commonly linked to late-onset forms. How these pathogenic substitutions affect the catalytic functions of aSyn fibrils has yet to be studied.

1.1 Aim

In this thesis, the principal objective was to evaluate whether aSyn amyloid fibrils of WT and those carrying glutamic acid-46-lysine (E46K), histidine-50-glutamine (H50Q), or alanine-53-threonine (A53T) mutations, exhibit catalytic behavior. Amyloid fibrils were prepared by seeded aggregation and their formation was verified through Thioflavin-T (ThT) fluorescence, circular dichroism (CD), and atomic force microscopy (AFM). The catalytic activity of all aSyn variants were then studied with various hydrolysis assays. These were (i) esterase assay which measured the hydrolysis of a model substrate paranitrophenyl acetate (pNPA), (ii) phosphatase assay which measured the de-phosphorylation of a model substrate paranitrophenyl phos-

phate (pNPP) and finally (iii) ATPase assay which measured the de-phosphorylation of a biologically relevant substrate adenosine 5'-triphosphate (ATP). All assays were used for all four variants. The results were evaluated whether a specific residue changes the catalytic function significantly.

2
Theory

2.1 Parkinson's Disease

Parkinson's disease affects over ten million people around the world [1]. As the population ages, these numbers are expected to increase. Among all neurodegenerative disorders, Parkinson's is the second most common after Alzheimer's disease (AD), highlighting its significant and growing impact on public health. While the probability of developing PD increases rapidly after the age of 65, the most common age for the PD diagnosis is between 55 and 65, and four percent of cases are diagnosed before the age of 50 [1], [9]. Men are approximately 1.5 times more likely to be affected than women. With aging population, cases are expected to rise from over 10 million today to 12-17 million by 2040 [10].

Over the past two centuries, the understanding of PD has evolved from focusing only on visible movement impairments to recognizing progressive loss of dopaminergic neurons in the substantia nigra, which causes nerve cells to die long before symptoms appear. This eventually leads to impaired voluntary movement and mood regulation [4]. The hallmark of the disease is the presence of Lewy bodies, insoluble α-Synuclein amyloid aggregates, which first appear in the olfactory bulb and brainstem, causing subtle non-motor disturbances years before tremor, rigidity, or bradykinesia appear [4], [11]. The early signs include also diminished sense of smell, chronic constipation, mood changes, and dream enactment behaviors, which could offer a critical window for detecting disease at a stage when interventions might slow or alter the progression of the disease [4]. Once Lewy bodies reach the substantia nigra, motor symptoms appear. PD is primarily diagnosed by observing bradykinesia, characterized by slow, decrementing movements, as well as rigidity or a resting tremor. There is currently no cure; therapies (medications, surgery, rehabilitation) focus solely on symptom management [12].

2.1.1 Cellular Hallmarks of Parkinson's Disease

Beyond the accumulation of α-synuclein and the formation of Lewy bodies, several interrelated cellular processes contribute to the pathophysiology of PD, one being the mitochondrial dysfunction. In PD, the electron transport chain's complex I is inhibited by toxins, inducing dopaminergic neurodegeneration and mitochondrial dysfunction [13]. This dysfunction leads to decreased ATP production and increased generation of reactive oxygen species (ROS), causing neuronal damage [13].

Besides mitochondrial dysfunction, dopamine metabolism further elevates intracellular ROS, leading to more oxidative stress, damaged lipids, proteins, and nucleic acids [14]. Dopaminergic neurons in the substantia nigra are especially prone due to their high metabolic activity and dopamine content, which can auto-oxidize to form toxic quinones (highly oxidative reactive products) [14]. This oxidative environment plays a causal role in driving the neuronal degeneration characteristic of PD.

Another contributing factor to PD's pathophysiology is DNA damage which arises from oxidative stress affecting both mitochondrial and nuclear DNA [15]. The accumulation of such damages impair cellular function and can trigger apoptotic pathways [15]. Several PD-related genes, including SNCA, LRRK2, PRKN, and PINK1, are involved in protecting the genome or repairing DNA damage [15]. Mutations in these genes weaken the cell's ability to repair the DNA, making neurons more vulnerable to damage [15].

Finally, disruptions in metal homeostasis have also been implicated in the pathophysiology of PD [16]. Abnormal deviations of metals, particularly increased iron content in subtantia nigra are present in PD [16]. Iron does not only increase oxidative damage but also promotes aSyn aggregation, linking metal dyshomeostasis to the core pathological features of PD. Copper, on the other hand, has been found to be increased in the cerebrospinal fluid, while decreased levels have been found in areas including substantia nigra, locus coeruleus, and cortex [16]. Other metals, such as zinc and manganese also play important roles. Excessive manganese exposure contributes to dopaminergic neurodegeneration by promoting oxidative stress, mitochondrial dysfunction, and disruption of metal homeostasis in vulnerable brain regions [16]. Zinc may have a dual effect, with systemic zinc deficiency potentially increasing oxidative stress and neurodegeneration, while region-specific zinc accumulation may contribute to damage in dopaminergic neurons [16].

2.2 α-Synuclein

α-Synuclein, composed of 140 amino acids with a molecular mass of 14.46 kDa [17], is neuronal protein which abnormal aggregation causes both the inherited and sporadic forms of Parkinson's disease [11]. aSyn is intrinsically disordered monomer, which adopts structure based on its environment, but upon aggregation it transforms into β-sheet–rich amyloid fibrils [3]. Structurally, α-synuclein can be divided into three regions: an amphipathic N-terminal segment (∼residues 1–60), a highly hydrophobic non-amyloid-β component (NAC) domain (∼residues 61–95) that nucleates cross-β fibril formation, and an acidic C-terminal tail (∼residues 96–140) [11].

Furthermore, α-synuclein amyloids exhibit significant polymorphism, adopting distinct structural arrangements influenced by factors such as pH, ionic strength, mutations, temperature, and external stresses, such as agitation and toxins [11]. High-resolution studies, including cryo-electron microscopy and solid-state NMR, categorize these fibrils mainly into straight and twisted forms [11]. Although both fibrils share a parallel, in-register β-sheet core organized into a five-layered β-sandwich,

their architectures differ because the protofilament align differently [11]. Straight fibrils have protofilaments aligned unidirectionally, while twisted fibrils involve protofilaments intertwining. This structural diversity can impact Parkinson's disease pathology, as different polymorphs may vary in toxicity and propagation in neural tissues [11].

The genes associated with monogenic Parkinson's disease can be classified by inheritance pattern. Mutations of autosomal dominant forms are linked to the gene SNCA, where a single mutated copy is sufficient to cause disease [8]. The SNCA gene encodes the α-synuclein which is central to the formation of Lewy bodies [18]. Mutations or multiplications in SNCA are linked to familial forms of Parkinson's disease. Several missense mutations in the SNCA gene have been linked to familial forms of parkinsonism, including A18T, A29S, A30P, E46K, H50Q, G51D, A53T, and A53E [8]. These mutations occur within the 140-amino-acid sequence of α-synuclein, the protein product of SNCA. In this work, the focus is on three of these pathogenic variants, A53T, E46K, and H50Q. Their locations within the α-synuclein sequence, along with the corresponding structural regions, are illustrated in Figure 2.1.

Figure 2.1: Structural regions of α-synuclein based on PDB entry 6A6B [19]. The N-terminal region includes residues 1–36, the fibril core residues 37–99, and the C-terminal region residues 100–140. Mutated residues studied in this work, i.e. Glu46, His50, and Ala53, are highlighted in yellow.

Structural studies of α-Synuclein fibrils have revealed that familial Parkinson's disease mutations result in distinct fibril conformations with potential functional consequences [8], [20], [21]. Table 2.1 summarizes structural data for α-Synuclein variants linked to familial Parkinson's disease, highlighting their fibril formation conditions [22]. These mutations (A53T, E46K, H50Q) lead to distinct polymorphs that may influence not only aggregation but also catalytic activity by altering structural exposure or electrostatics. In this thesis, fibril formation was performed under similar pH conditions (pH 7.6), making the known structures a useful reference for understanding how mutation-driven conformational differences might relate to catalytic function.

Early-onset familial PD, onset in late 30s or 40s, can be caused by over expression of the aSyn protein or by the point mutations E46K A53T or A30P. Overexpression of aSyn is typically caused by extra copies of the wild-type gene [11]. In contrast, the H50Q point mutation and wild-type protein cause late-onset Parkinson's disease, which typically manifests in patients in their 60s [23].

PDB ID	Variant	Method	Res. (Å)	pH	Buffer (fibril formation)	notes
6LRQ	A53T	cryo-EM	3.5	7.4	50 mM Tris, 150 mM KCl	N-acetylated
6L4S	E46K	cryo-EM	3.37	7.5	50 mM Tris, 150 mM KCl	N-acetylated
6PES	H50Q	cryo-EM	3.6	?	15mM TBPBr	pH not available
6A6B	WT	cryo-EM	3.07	7.5	25 mM Tris–HCl	N-acetylated

Table 2.1: Representative cryo-EM structures of α-synuclein pathological variants, highlighting fibril formation conditions and pH [22]. One PDB entry per mutation is shown to illustrate details relevant to catalytic activity studied in this thesis.

2.3 Amyloid Fibrils

Amyloids are insoluble protein aggregates defined by a characteristic cross-β-sheet structure, where β-strands run perpendicularly to the fibril axis [24] as seen in schematic Figure 2.2. These aggregates form a amyloid fibrils, a specific type of fibrillar structure that appears in both pathological contexts (e.g. neurogenerative diseases) and functional biological systems (e.g., in biofilms) [2].

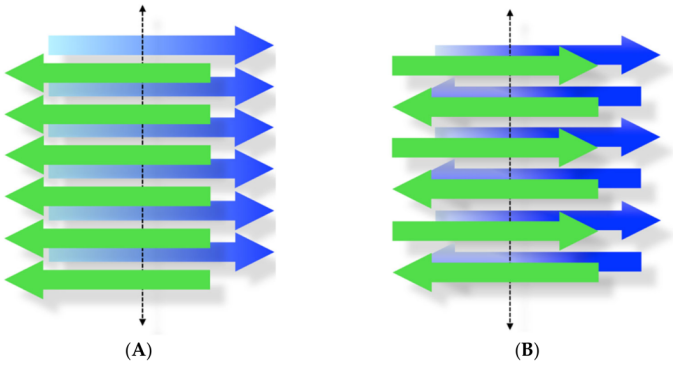

Figure 2.2: Common cross-β structures in amyloid fibrils [25]. In both parallel (A) and antiparallel (B) arrangements, β-strands (green and blue) align perpendicularly to the fibril axis (dotted line), forming the characteristic cross-β structure [25]. The fibrils are stabilized by non-covalent interactions, primarily backbone hydrogen bonding [25]

Amyloid fibril formation typically follows a sigmoidal kinetic profile characterized by three distinct yet overlapping phases: the lag phase (primary nucleation), the elongation phase, and the saturation phase [26], as illustrated in Figure 2.3. During the lag phase, soluble monomeric proteins undergo stochastic interactions that lead to the formation of small, unstable oligomeric nuclei [27]. This phase is typically slow and highly dependent on monomer concentration as well as solution conditions. It is thermodynamically unfavorable transition and is often the rate-limiting step of fibrillogenesis [28].

Once stable nuclei are formed, fibril growth goes into a rapid elongation phase, where

monomers attach to the ends of existing fibrils [28]. This elongation process is often modeled as a linear reaction and can proceed without further nucleation events. Unlike the nucleation phase, elongation process is thermodynamically favorable and is accelerated by secondary processes fragmentation and secondary nucleation [26].

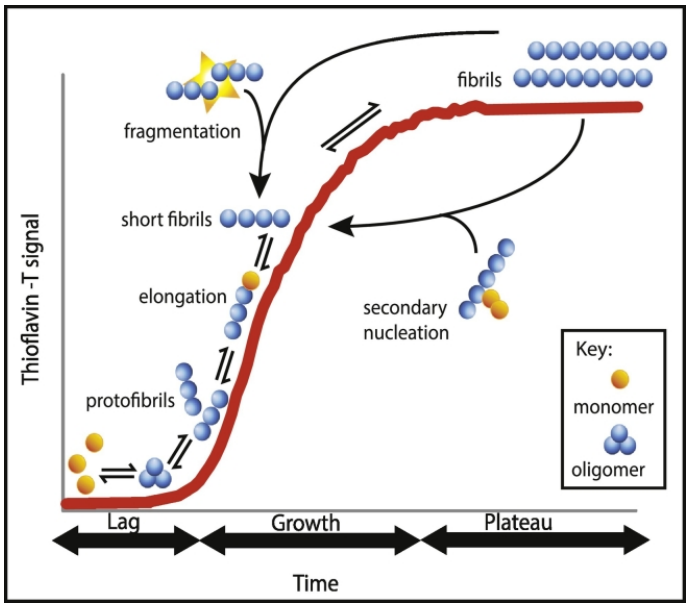

Figure 2.3: Schematic figure of amyloid formation kinetics. Lag phase consists of nucleation and oligomer formation, which is followed by elongation phase with fibril growth and secondary processes [26]. A saturation phase indicates steady state as monomer levels are depleted [26].

In fragmentation, existing fibrils break into smaller pieces, creating new growth points where monomers can attach to [27]. This process depends on aggregate mass and has a constant rate. On the other hand, secondary nucleation occurs when the surface of existing fibrils catalyze the formation of new nuclei from monomers. Secondary nucleation depends on concentration of free monomers and existing fibrils, leading to autocatalytic amplification of fibril formation [27]. These secondary processes exponentially increase the number of new aggregation sites [27] and is believed to play a critical role in the propagation of amyloid pathology in vivo.

Eventually, the system reaches a saturation or plateau phase, where the concentration of free monomers falls below a threshold required for fibril elongation [26]. At this stage, fibrils reach a stable equilibrium with minimal net growth. Each phase of amyloid formation contains all processes simultaneously but one typically dominates depending on environmental conditions [27].

2.4 Protein Expression and Purification

Plasmids are extrachromosomal DNA elements commonly present in bacteria, characterized as small, circular, double-stranded DNA molecules [29]. Due to their high

replication rates, plasmids, such as those derived from Escherichia Coli (E. Coli), have been used extensively in genetic engineering. Plasmids designed for transferring genes are often smaller than naturally occurring plasmids, which generally provides greater structural stability and higher transformation efficiency, i.e. successful uptake by the host bacterial cells. These plasmids contain their own replication origin and are relaxed, allowing them to replicate independently of the bacterial chromosome, unlike tightly regulated chromosomal origins [30]. This relaxed replication is ideal for efficient α-synuclein protein expression.

Vector plasmids typically include an antibiotic resistance gene for selecting bacteria that carry the plasmid, as well as a multiple cloning site (MCS) with unique restriction sites to insert the desired gene into [29]. Insertional inactivation of a marker gene allows the differentiation between plasmids with and without the insert.

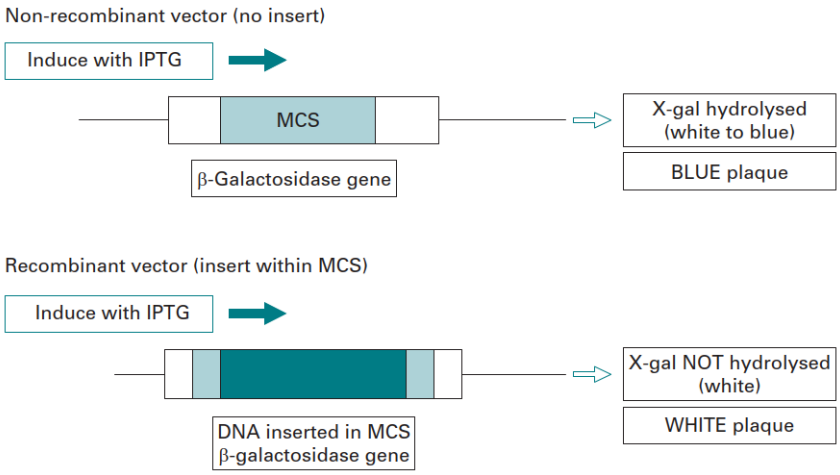

Figure 2.4: General overview of a screening method using IPTG-induced blue/white colony differentiation to detect successful plasmid recombination [29].

Plasmid uptake is typically achieved through heat shock or electroporation treatment [31], after which transformed bacterial colonies are selected based on antibiotic resistance [29]. To identify recombinant plasmids, a screening method called replica plating is often used [29], as seen in illustrative example in Figure 2.4. In replica plating, bacterial colonies are transferred to a second plate containing a different antibiotic. Only those with the desired plasmid will grow, making it easy to distinguish successful recombinants. After selecting the right colonies, protein expression is induced by chemical inducer, usually isopropyl β-D-1-thiogalactopyranoside (IPTG) in lac-based systems. This activates transcription from the lac operon and results in high-level production of protein, or in this case alpha-synuclein, in the transformed E. coli cells [32].

2.4.1 SDS-PAGE

Sodium dodecyl-sulfate polyacrylamide gel electrophoresis (SDS-PAGE) is the standard technique for determining protein sizes [29]. The anionic detergent SDS binds

at roughly one molecule per two amino-acid residues denaturating the protein into rod-shapes and covering the proteins' native charges with SDS' own charge. Now every protein has same charge and shape (due to repulsive charges), resulting in a similar charge-to-mass ratio, therefore migration through the gel matrix depends almost exclusively on molecular size. A set of marker proteins (e.g. one depicted in Figure 2.5) with known molecular weights (MW) are used to run alongside the sample for a visual determination. By plotting the distance each marker travels against the logarithm of its MW, a standard curve can be created. The migration distance of the unknown protein can then be used to estimate its MW from this curve.

Gradient gels are used in SDS-PAGE to separate wider range of proteins based on their MW by gradually decreasing pore size in the gel from top to bottom, allowing both small and large proteins to resolve effectively in the same run (wider range of MW) [29]. They also improve resolution between proteins with similar sizes by sharpening the bands as each protein slows at its pore-size limit. Electrophoresis is monitored with a bromophenol-blue tracking dye, and proteins are visualised after the run with rapid Coomassie or more sensitive silver staining.

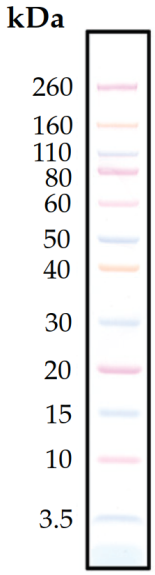

Figure 2.5: SDS-PAGE used in this thesis involves loading 10 µL of Novex® Sharp Pre-Stained Protein Standard onto a NuPAGE® 4–12% Bis-Tris Gel using MES SDS Running Buffer [33]. This setup allows for clear visualization of protein bands during electrophoresis, with the pre-stained standard providing MW markers ranging from 3.5 to 260 kDa.).

2.5 Analytic Methods

2.5.1 Thioflavin-T Fluorescence

Thioflavin T (ThT) is a benzothiazole dye widely used in biochemical research as a fluorescent probe to detect and quantify amyloid fibrils [34]. It is especially practical in studying protein aggregation linked to neurodegenerative diseases such as, PD. When free in solution, ThT exhibits weak fluorescence, but upon binding to amyloid fibrils, its fluorescence intensity significantly increases, making it a reliable indicator of amyloid formation. When ThT binds to amyloid fibrils, it absorbs light at approximately 440 nm, which excites the molecule to a higher energy state. After excitation, ThT releases energy as fluorescence, with a peak emission around 490 nm [34]. This fluorescence is significantly enhanced when ThT is bound to amyloid fibrils compared to when it is free in solution. On the other hand, an unbound ThT exhibits minimal fluorescence, with its excitation and emission peaks occurring at lower wavelengths, approximately 350 nm and 440 nm, respectively [34].

Optimal ThT concentration for detecting fibrils lies between 20–50 µM, as higher concentrations result in fluorescence saturation rather than increased sensitivity [35]. ThT at concentrations up to 20 µM has negligible impact on aggregation. However, at concentrations of 50 µM or higher, ThT may alter aggregation kinetics in a protein-dependent manner.

2.5.2 Circular Dichroism

Circular dichroism (CD) spectroscopy is an optical technique used to measure the differential absorption of left- and right-circularly polarized light by chiral (optically active) molecules [36]. This differential absorption is detected due to the asymmetric environment of light-absorbing group and is expressed as the difference in absorbance; $\Delta A = A_L - A_R$, where A_L and A_R are the absorbance values for left- and right-circularly polarized light [36]. The differential absorption results in elliptically polarized transmitted light, which can be quantified and described as ellipticity $(\theta, mdeg)$.

CD is useful tool in the analysis of protein secondary structures, due to the characteristic spectral signatures produced by the peptide backbone in the far-UV region (190–250 nm) [37]. α-helices show two negative peaks at 208 nm and 222 nm, and a positive maximum near 190 nm as seen in Figure 2.6. β-sheets produce a negative peak close to 218 nm and a positive one close to 195 nm, while random coils exhibit a single broad negative peak near 198 nm [37]. These signals arise from how the protein's structure affects its absorption of light, allowing different shapes like helices and sheets to be distinguished.

CD measurements are performed in optically transparent cuvettes, usually made of quartz, to avoid interference with UV transmission [36]. Protein concentration in CD studies can be determined using Beer-Lambert's law when the data is recorded

in absorbance [38]:

$$C = \frac{A}{\varepsilon \cdot d} \tag{2.1}$$

where:

- C = molar concentration (mol/L),
- ΔA = absorbance at a specific wavelength,
- ϵ = molar extinction coefficient (M^{-1} cm^{-1})),
- d = path length of the cuvette (cm).

To convert CD data from differential absorbance to ellipticity, the following relationship is used:

$$\theta(\text{degrees}) = \Delta A \times \left(\frac{4}{\ln 10}\right) \times \left(\frac{180}{\pi}\right) \approx \Delta A \times 32.982 \tag{2.2}$$

In order to compare data across experiments and proteins of different sizes, the observed ellipticity is often normalized into the Mean Residue Ellipticity (MRE):

$$\theta_{\text{MRE}} = \frac{100 \cdot \theta_{\text{obs}}}{C \cdot l \cdot N} \tag{2.3}$$

where:

- θ_{MRE} = Mean Residue Ellipticity ($\text{deg} \cdot \text{cm}^2 \cdot \text{dmol}^{-1}$),
- θ_{obs} = Observed ellipticity (mdeg),
- C = Protein concentration (mol/L),
- l = Path length of the cuvette (cm),
- N = Number of amino acid residues.

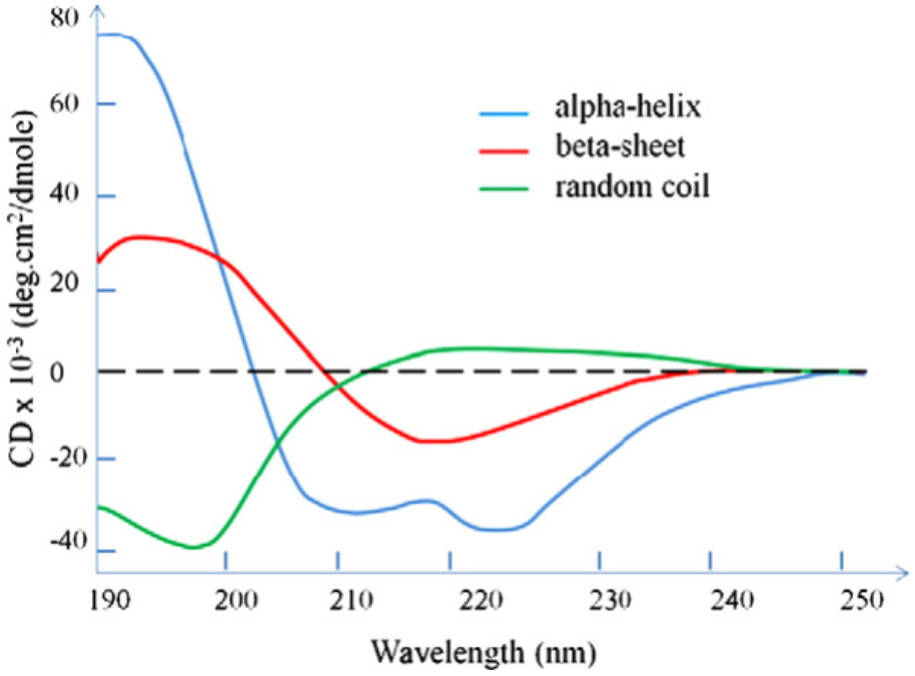

Figure 2.6: Comparison of CD spectral features across different wavelength regions [37]. The curves represent characteristic CD spectra for proteins predominantly adopting a single type of secondary structure (α-helix, β-sheet, or random coil).

2.5.3 Atomic Force Microscopy

Atomic force microscopy (AFM) offers a way to examine proteins and protein assemblies on surfaces under ambient conditions without the vacuum or high-energy electron beams for electron microscopy [39]. AFM uses a sharp probe attached to a flexible cantilever that scans across a sample in a raster pattern, measuring either direct contact forces (contact mode) or intermittent contacts (tapping mode). These two modes differ in how the tip interacts with the sample: contact mode maintains continuous tip-surface contact in the repulsive force regime, while tapping mode oscillates the cantilever at resonance frequency to periodically touch the surface, thereby minimizing sample distortion. A laser beam is directed at the cantilever's back surface, and the reflection is captured by a position-sensitive detector to monitor cantilever deflection as the tip scans over the sample.

High-resolution AFM images offer a detailed view of sample topography and shape at the nanometer level, making it possible to discern subtle features of fibrillar protein structures [39]. This degree of detail helps to confirm that the aSyn amyloid fibrils produced align with the expected morphology, including their characteristic filament dimensions. By examining parameters such as height profiles, width distributions, and overall arrangement; AFM can help detect any anomalies, incomplete assemblies, or misfolded aggregates. As a result, the method does not only verify correct fibril formation but also provides insights that guide improvements in sample preparation and imaging protocols, ensuring consistent and reproducible results.

2.5.4 Esterase Activity Assay

Esterase-like behavior of aSyn amyloid fibrils can be assessed by employing para-nitrophenyl acetate (pNPA) as a model substrate, where the cleaved product (para-nitrophenol, pNP) is readily detected at 410 nm. Cleavage occurs at the ester linkage between the acetyl group and the aromatic ring, a reaction facilitated by the electron-withdrawing nitro group. Figure 3.1 depicts the ester hydrolysis reaction central to this assay.

2.5.5 Phosphatase Activity Assay

Phosphatase-like activity of aSyn amyloid fibrils can be evaluated using para-nitrophenyl phosphate (pNPP) as a model substrate. During this reaction, the phosphate group is cleaved, yielding para-nitrophenol (pNP), which is easily monitored at 410 nm. Figure 3.1 illustrates the phosphate hydrolysis reaction that underpins this assay.

2.5.6 ATPase Activity Assay

ATPase activity can be evaluated by monitoring the hydrolysis of adenosine 5'-triphosphate (ATP), an energy-carrying molecule with particular biological relevance, as opposed to the synthetic substrate pNPP or pNPA. ATP consists of a three phosphates linked by high-energy phosphodiester bonds. When these bonds are broken, ATP is converted to ADP or AMP, releasing inorganic phosphate (P_i)

or pyrophosphate (PP_i). Figure 3.1 illustrates this dephosphorylation process.

The Malachite Green assay is used to quantify free phosphate by forming a phosphomolybdate complex, which then reacts with malachite green to produce a color signal detectable at 610 nm. However, this method does not detect pyrophosphate, meaning any direct cleavage to AMP remains undetected. Employing ATP in this assay thus provides a more physiologically relevant measure of phosphatase-like activity in aSyn amyloid fibrils compared to pNPP and pNPA, which serve primarily as a convenient model substrate.

2.5.7 Enzyme Kinetics

Michaelis–Menten (MM) kinetics offer a fundamental framework for understanding how the rate of an enzyme-mediated reaction varies as a function of substrate concentration [40]. In its simplest model, the enzyme (E) reversibly binds the substrate (S) to form an enzyme–substrate complex (ES), which then either reverts back to E+S or proceeds to generate the product (P). The rate equation can be derived under the assumption that the chemical conversion of ES into product is the rate-limiting step:

$$\text{Michaelis–Menten equation:} \quad v = \frac{V_{\max}[S]}{K_m + [S]}$$

where v is the observed reaction velocity at a given substrate concentration $[S]$.

A saturation plateau emerges at high $[S]$, signifying that all available enzyme is bound to substrate. This maximal velocity is denoted by $V_{\max}$. Experimentally, these parameters can be obtained by measuring initial reaction velocities across a range of substrate concentrations and fitting the data to the MM equation. Parameters such as K_m (the substrate concentration at which the velocity is half $V_{\max}$) and $V_{\max}$ reveal how tightly the enzyme (or enzyme-like entity) binds the substrate and the upper limit of its catalytic speed. This approach thus provides insights into the reaction mechanism and enzymatic efficiency, whether studying classical enzymes or protein assemblies with potential catalytic activity. The resulting MM relationship is visualized in Figure 2.7.

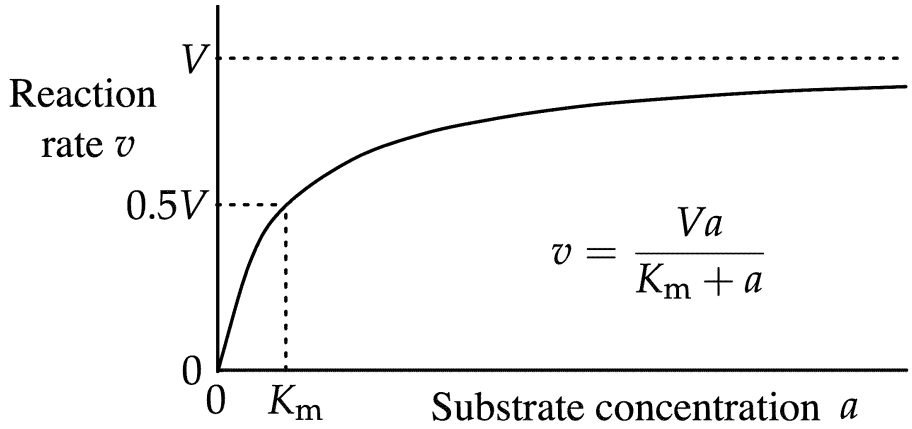

Figure 2.7: Michaelis-Menten plot showing initial reaction velocity velocity as a function of substrate concentration.

3
Methods

3.1 Protein Expression and Purification

3.1.1 Transformation of E. coli with Expression Plasmids

The plasmids of α-Synuclein protein (WT and variants) were introduced into *TOP10 Escherichia coli* through standard bacterial transformation protocols. This was performed by mixing the plasmid DNA encoding α-Synuclein protein with chemically competent *E. coli* cells and then subjected to heat-shock for 30 seconds in 42°C to facilitate the plasmid intake. This was followed by a one-hour recovery in an antibiotic-free medium. Then the cells were spread on agar plates containing the appropriate antibiotic to select for successful colonies, which appeared as colonies after overnight incubation at 37°C. After plasmid propagation, the purified plasmid DNA was transformed into E. Coli BL21 (DE3) competent cells.

3.1.2 Protein Expression in E. coli

To express α-Synuclein in Luria Broth (LB), a single transformant colony was used to inoculate a small starter culture, which was grown overnight at 37°C with shaking of 200-250 rpm. The overnight culture was then diluted into fresh growth medium and incubated until the optical density at 600 nm (OD_{600}) reached approximately 0.5. At that point, protein expression was induced with 0.5 mM IPTG (Isopropyl β-d-1-thiogalactopyranoside). Induced cultures were left to grow for 15–18 hours at 20°C. After induction, cells were harvested by centrifugation at 8000 g for 10-15 minutes, then collected pellets were either used immediately or stored at -20°C for future processing.

3.1.3 Protein Purification and Analysis

Cells from the pellet were resuspended in 20 mM Tris-HCl (pH 8.0). Lysis was performed on ice by sonication for 30 min with altenrating pulses in the presence of a protease inhibitor cocktail. To minimize viscosity from nucleic acids, DNase I (1–10µg/mL) was added to the mixture following the sonication, and the sample was incubated on ice for 15 minutes. The resulting cell lysate was then subjected to a 95°C heat treatment for 10 minutes to facilitate the precipitation of numerous host proteins, leaving α-Synuclein primarily in solution. The mixture was subsequently centrifuged at 16 000 g for 30 minutes, and the clear supernatant was filtered through a 0.22 µm membrane prior to chromatography.

Anion exchange chromatography using a Q Sepharose column served as the first purification step. The column was equilibrated with Buffer (20 mM Tris-HCl, pH 8.0), and the filtered cell lysate was loaded at a controlled flow rate. After unbound material was washed off with the first buffer, an elution gradient was applied, transitioning from the first to second buffer (20 mM Tris-HCl, pH 8.0, 1 M NaCl). Fractions were collected across the gradient, and those containing the highest concentrations of α-Synuclein were identified through SDS-PAGE analysis on a 4–12% SDS-PAGE gradient gel form, which provides a polyacrylamide gradient (lower % for larger proteins, higher % for smaller proteins) to improve resolution across a wide range of molecular weights. A pre-stained protein molecular-standard was used to estimate molecular weights in SDS-PAGE. This standard marker was loaded at 10 µL in first well, whereas 20 µL of each sample (load, flowthrough and column fractions) were loaded in rest of the wells. Gels were typically stained briefly with a rapid "instant blue" dye for a quick confirmation, followed by more traditional Coomassie staining for a clearer visualization of protein bands.

Selected α-Synuclein-containing fractions were pooled and further purified by size-exclusion chromatography on a HiLoad 16/600 Superdex 75 column equilibrated with 20 mM Tris-SO_4 (pH 7.4). At a flow rate of 1 mL/min, protein typically eluted as a single major peak. The α-Synuclein peak was confirmed by monitoring absorbance at 280 nm. After pooling these fractions, the protein was concentrated using ultra centrifugal concentrator to approximately 2 mg/mL. The ratio of absorbance at 260 nm and 280 nm was kept below 1.0 to ensure minimal nucleic acid contamination. The purified and concentrated α-Synuclein was finally aliquoted into small volumes, flash-frozen, and stored at -80°C.

3.2 Preparation of α-Synuclein Amyloid Fibrils and Seeds

3.2.1 Gel Filtration

Fresh aSyn fibrils were prepared immediately before each assay. Aliquots of aSyn, stored at -80°C, were thawed and concentrated using 10 kDa MWCO filter (13,400 rpm, 5 min), after which the protein was loaded into a Superdex 75 10/300 column equilibrated with TBS buffer (20 mM Tris, 150 mM NaCl, pH 7.6) in order to obtain homogeneous monomeric solution. The aSyn concentration was determined by integrating the peak area at 280 nm using extinction coefficient of 0.412 (mg $mL^{-1})^{-1}$ cm^{-1} assuming molecular mass of 14.46 kDa. The fractions corresponding to the absorbance peak at 280 nm were pooled. These monomeric fractions served both as the control sample and as the starting material for amyloid fibril formation.

3.2.2 Thioflavin-T Fluorescence

The gel-filtered monomers from all variants were aggregated into amyloid fibrils using a two-step process. First, gel-filtered monomers were placed in a 96-well half-area plate containing glass beads. The plate was then incubated at 37°C in a BMG Labtech Fluorstar Optima plate reader with continuous agitation for 2-4 days. To monitor the aggregation process, three wells were treated with Thioflavin T (final mixture concentration: 20 µM), enabling fluorescence-based tracking of the amyloid fibril formation curve. The initial monomer concentrations used for aggregation were 82 µM (WT), 134 µM (E46K), 140 µM (H50Q), and 85 µM (A53T). Preformed fibril seeds were added to some of the samples at 5–10% relative to the total monomer concentration in the final mixture, while the rest underwent unassisted aggregation.

Once the aggregation curve reached saturation, the samples were collected and centrifuged at 13,400 RPM for 30 minutes. This step resulted in the formation of a pellet, which was retained, while the supernatant containing monomeric, dimeric, and trimeric forms of the protein was removed. To quantify the remaining monomer concentration in the supernatant, it's absorbance at 280 nm (corresponding to four tyrosine residues in aSyn) was measured. Using the molar extinction coefficient for aSyn (ε_{syn} =5600 $M^{-1}cm^{-1}$), the monomer concentration was determined, allowing indirect calculation of the pellet's fiber concentration. The pellet was then resuspended to a final concentration of 200 µM, flash-frozen in liquid nitrogen, and stored at -80°C.

In the second step, freshly gel-filtered monomers were incubated with preformed amyloid fibrils that had been previously flash-frozen. The seed concentration ranged from 5-10% relative to the monomer concentration. The mixture was transferred to a microcentrifuge tube and incubated at 37°C in a bench-top incubator for 3-4 days to promote seeded fibril growth. After incubation, the same centrifugation protocol was applied to separate fibrils from unincorporated protein. The pelleted fibrils were then resuspended to the desired concentration for subsequent enzymatic assays.

3.2.3 Circular Dichroism

The aSyn amyloid fibril samples of WT, E46K, H50Q, and A53T used in the enzymatic assays were diluted to a final fibril concentration of 10 µM using Milli-Q water. CD spectroscopy was performed using a Chirascan Circular Dichroism Spectrometer to record spectra in the wavelength range of 190–250 nm. This range was selected to confirm the secondary structure of the fibrils, ensuring the presence of a β-sheet conformation rather than a random coil or monomeric state. The characteristic β-sheet structure was identified by a distinct positive peak at approximately 198 nm and a prominent negative peak around 217 nm.

3.2.4 Atomic Force Microscopy

AFM was used to characterize the morphology of the amyloid fibrils. The sample was prepared by diluting aggregated fibrils from 200 µM to 10 µM with Milli-Q

water. A 100 µL of this diluted sample was placed onto a freshly cleaved mica plate and left to incubate for 15–20 minutes at room temperature. Following incubation, excess liquid was removed with a tissue, and the plate was rinsed by adding 100 µL of Milli-Q water. This rinse-and-dry step was repeated 4–5 times to thoroughly wash away unbound material. Finally, the mica plate was dried using a gentle stream of nitrogen gas. AFM images were acquired using an NTEGRA Prima instrument equipped with a gold-coated single-crystal silicon cantilever, and all image processing and analysis were carried out using WSxM 4.0 beta 10.0 software [41].

3.3 Colorimetric Enzyme Assays

All activity assays implemented in this work, esterase, phosphatase, and ATPase, were based on already established protocols. Figure 3.1 presents a schematic overview of each substrate, the specific bonds cleaved, the buffers used, and the absorbance wavelengths monitored. In these experiments, pNPA served as the ester substrate, pNPP was the phosphate donor, and ATP was used in the ATPase assay.

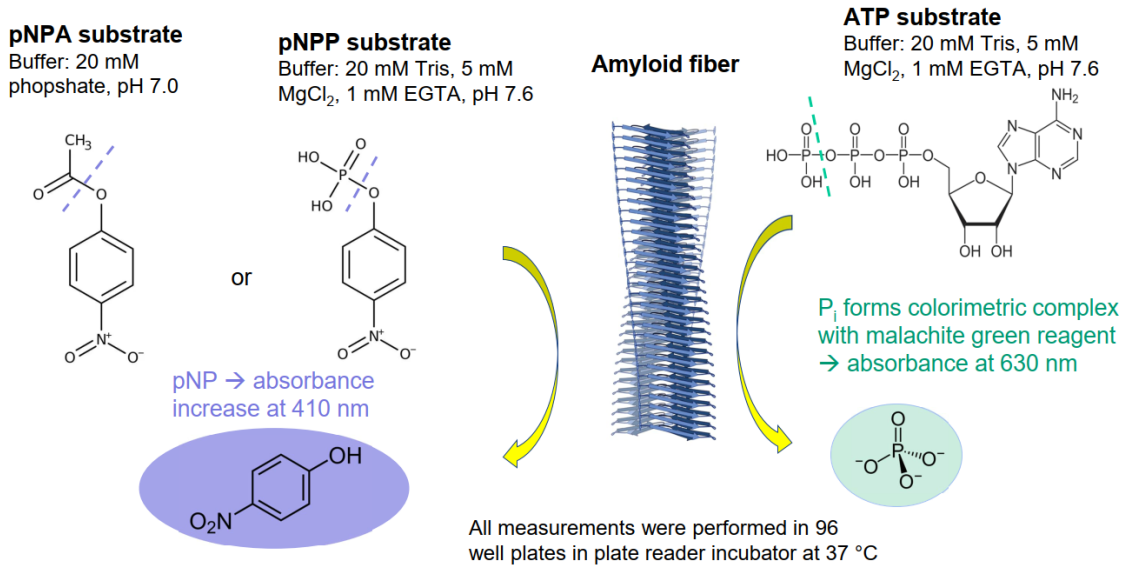

Figure 3.1: Schematic overview of the spectrophotometric activity assays used in this work. The diagram displays the three chromogenic substrates, pNPA (esterase assay), pNPP (phosphatase assay) and ATP (ATPase assay), together with their reaction buffers, dashed scissile bonds and optical detection wavelengths. pNPA in 20 mM phosphate buffer (pH 7.0) is hydrolysed to pNP and monitored at 410 nm; pNPP and ATP, both in 20 mM Tris, 5 mM $MgCl_2$, 1 mM EGTA (pH 7.6), respectively release pNP (410 nm) and inorganic phosphate, the latter forming a malachite-green complex detected at 630 nm. All assays were conducted in 96-well plates at 37 °C using a temperature-controlled plate reader.

3.3.1 Esterase Activity Assay

Fresh pNPA stock solutions were prepared (100 µM dissolved in acetonitrile) and then diluted in 20 mM phosphate buffer (pH 7.0) to generate a range of substrate concentrations. The resulting mixtures were combined with 20 µM of fibrillar aSyn (WT, E46K, H50Q and A53T), while blanks were made identically but without aSyn fibrils; buffer was used instead.

All samples were placed in 96-well, half-area plates (Corning) with a nonbinding surface, and absorbance at 410 nm was measured every three minutes for 70 min using a Fluorostar Optima plate reader. Because pNP formation directly correlates with enzyme-like activity, the absorbance readings were converted to concentrations using an extinction coefficient of 7500 $M^{-1}\,cm^{-1}$. The concentration of the blank samples was used to remove the background absorbance. After verifying linearity in the initial phase of the reaction, the first 20 minutes of data were fitted to the Michaelis–Menten model to calculate the kinetic parameters $V_{\max}$ and K_m.

3.3.2 Phosphatase Activity Assay

The phosphatase assay was performed similarly to the esterase assay, except that *p*-nitrophenyl phosphate (pNPP) was used as the substrate. pNPP was dissolved in a buffer containing 20 mM Tris (pH 7.6), 5 mM $MgCl_2$, and 1 mM EGTA. The extinction coefficient for for converting the absorbance values to concentration was 13,500 $M^{-1}\,cm^{-1}$.

3.3.3 ATPase Activity Assay

The ATPase assay was used to monitor the dephosphorylation of ATP to ADP using malachite green dye. In this reaction, the free monophosphate first reacts with ammonium molybdate to form a phosphomolybdate intermediate, which subsequently interacts with malachite green to generate a colorimetric complex. This complex is detectable at 630 nm. The buffer used in this assay was 20 mM Tris (pH 7.6), 5 mM $MgCl_2$, and 1 mM EGTA). An eight point phosphate standard series (0-40 µM) was measured in technical duplicates, and the slope resulting from linear regression was used as the conversion coefficient for calculating the phosphate concentrations in the samples. The same procedure was applied to aSyn monomers/background to verify their lack of catalytic activity. Reactions were incubated in 96-well half-area plates, and at defined time points, the samples were frozen to stop the reaction. Later malachite green reagent was added to stop the reaction and develop color. The resulting absorbance at 630 nm was converted to phosphate concentration using the calibration curve.

4

Results

4.1 Protein purification

All four aSyn variants were expressed in E. coli at high and soluble yields. Peak fractions from ion-exchange chromatography contained thick band at 15 kDa on SDS-PAGE, confirming expected monomeric size. Slight fragmentation on SDS-PAGE was observed generally with A53T variant, but no indication of dimer or trimer formation. The three most highest aSyn containing fractions were chosen for the next step. Size-exclusion chromatography (SEC) yielded usually a single symmetrical peak for all variants. Occasionally a slight trailing shoulder was seen in some experiments, again indicating fragmentation. These fractions were discarded. Figure 4.1 displays representative SDS-PAGE and SEC profiles for each variant.

4.2 Thioflavin-T Fluorescence

In Figure 4.2, normalized ThT fluorescence curves illustrate the aggregation kinetics of each variant (WT, E46K, H50Q, and A53T). The A53T variant compares two aggregation methods used in this study: seeded aggregation and aggregation with glass beads, highlighting the absence of an initial lag phase in the first method. The graphs shows WT and H50Q aggregation using glass beads, whereas the graph for E46K shows aggregation with seeds, showing the aggregation going straight to growth phase. In all cases, aSyn monomers successfully aggregated into amyloid fibrils, reaching saturation. The final graph in the Figure 4.2 demonstrates the aggregation kinetics of a sample that was treated with ThT after being incubated on a bench incubator, confirming that this method also leads to complete aggregation. In all experiments the ThT concentration was approximately 20 µM.

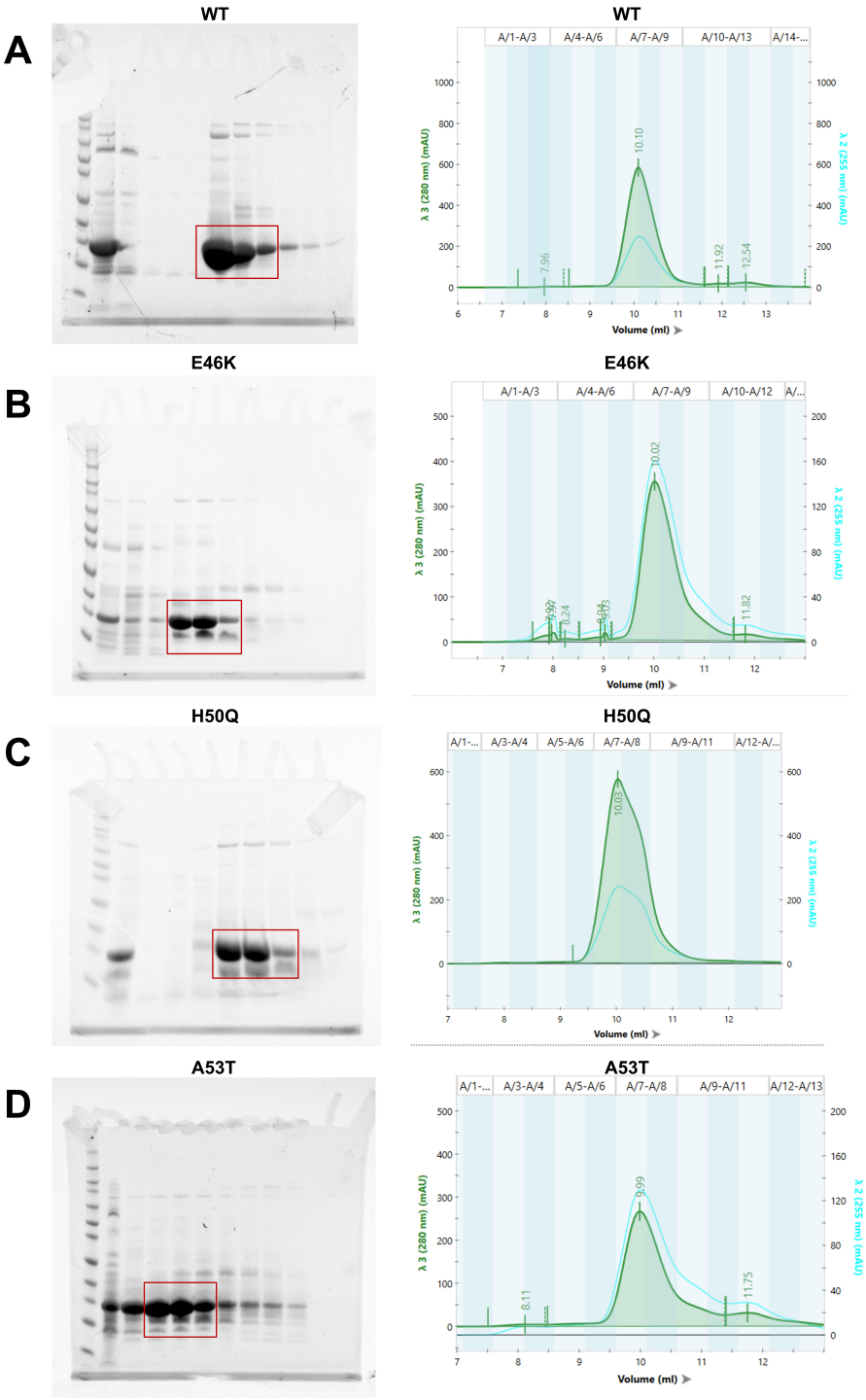

Figure 4.1: SDS–PAGE and SEC of the four aSyn variants. Each horizontal panel corresponds to one variant (WT, E46K, H50Q, A53T). In SDS-PAGE, the left-most lane contains molecular-weight marker; red boxes highlight the bands corresponding 15 kDa. Fractions in boxes were chosen for further experiments. In SEC, the green trace is the A_{280} (protein) while the blue trace is A_{255} (nucleic acid). The two highest fractions (A/7,A/8) were used as starting material for amyloid formation and as control group.

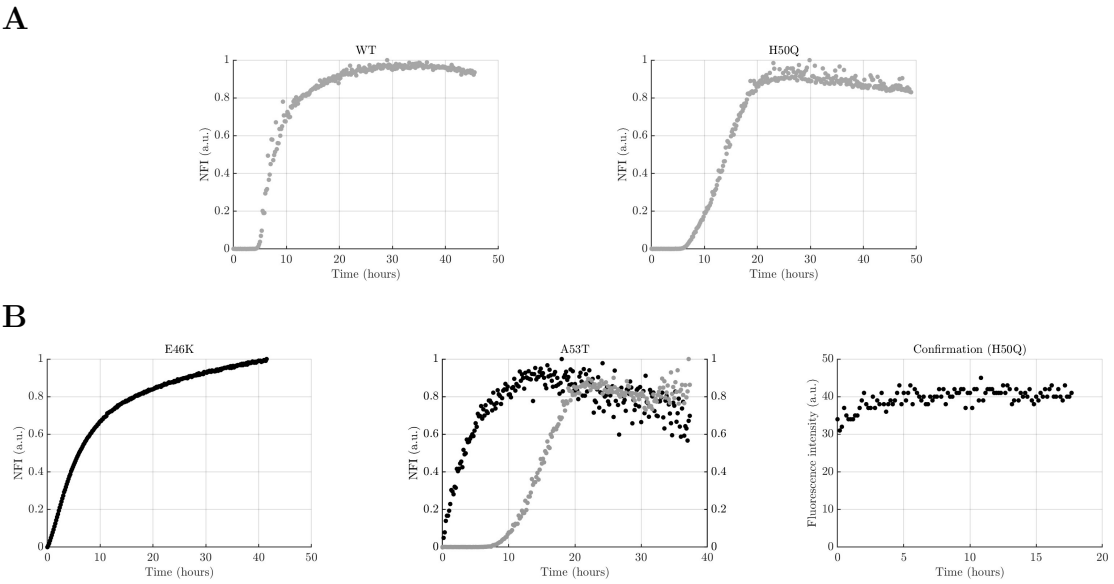

Figure 4.2: ThT fluorescence profiles of all aSyn variants. Panel A shows aggregation of monomers without seeds (WT and E46K), while Panel B presents seeded aggregation experiments for H50Q, A53T, and a confirmation experiment for H50Q. Black dots represent reactions with seeds and grey dots represent aggregations without seeds. All fluorescence values are normalized, except for the H50Q confirmation, which presents absolute intensity values from bench-top incubation to demonstrate the saturation of the aggregation process.

4.3 Circular Dichroism

CD spectra were measured for all fibril samples that were used in enzymatic activity assays. Figure 4.3 presents a spectrum of one sample for each variant, which is consistent with the typical results observed across all CD measurements. The spectra were recorded in the wavelength range of 190–250 nm.The characteristic shape of the CD curves confirm the presence of a β-sheet structure in the samples, as evidenced by a positive peak near 198 nm and a negative peak around 217 nm. This indicates successful aggregation of the samples, as no spectral features associated with monomeric or random coil structures were observed.

The amplitude of the spectra varies among the different variants, likely due to differences in sample purity and cuvette conditions. The results for A53T variant exhibits a lower amplitude in the positive peak, suggesting that additional measurements would be recommended to do for improved results. However, the overall spectral profiles strongly support the presence of a β-sheet structure in all samples.

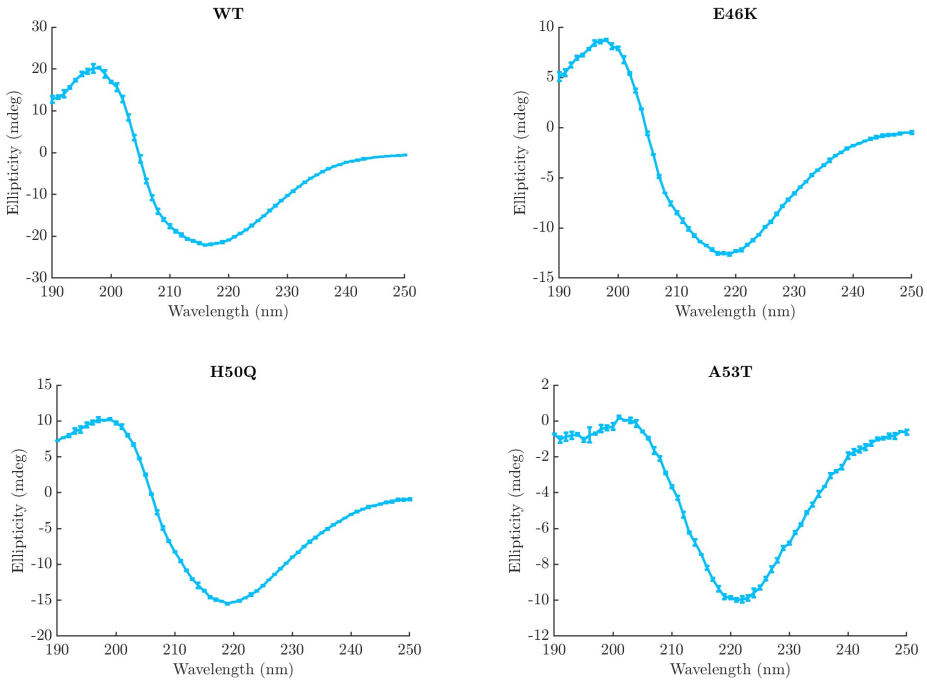

Figure 4.3: CD spectra of all experimented variants. The concentration of the all sample was 10 µM of fibrils resuspended in Milli-Q water.

4.4 Atomic Force Microscopy

Figure 4.4 shows the AFM images of amyloid fibrils from each variant. In all cases, the fibrils appear predominantly elongated and unbranched. To ensure consistency, regions where fibrils overlapped were avoided during diameter and periodicity measurements. The quantitative results are summarized in the Table 4.1, where diameter was measured at three different locations on each fibril, and periodicity was evaluated at two locations.

Among the variants, WT and A53T exhibited higher average periodic spacings (71.0 nm and 71.4 nm, respectively) compared with E46K (57.8 nm) and H50Q (64.5 nm). In contrast, the diameter was less consistent within the variants. H50Q showed the smallest average diameter (4.3 nm), while A53T had the largest (6.6 nm). WT and E46K fell between these, with diameters of 5.5 nm and 5.9 nm, respectively.

In the Figure 4.5, the fibril's height profile is presented, and its overall height was determined by measuring the difference between the maximum and minimum values along the profile. To identify the fibril's periodicity, the longitudinal height data were analyzed using MATLAB's `findpeaks` function. Various parameter settings were tested to optimize the results, aiming for the most accurate and automated approach to periodicity detection.

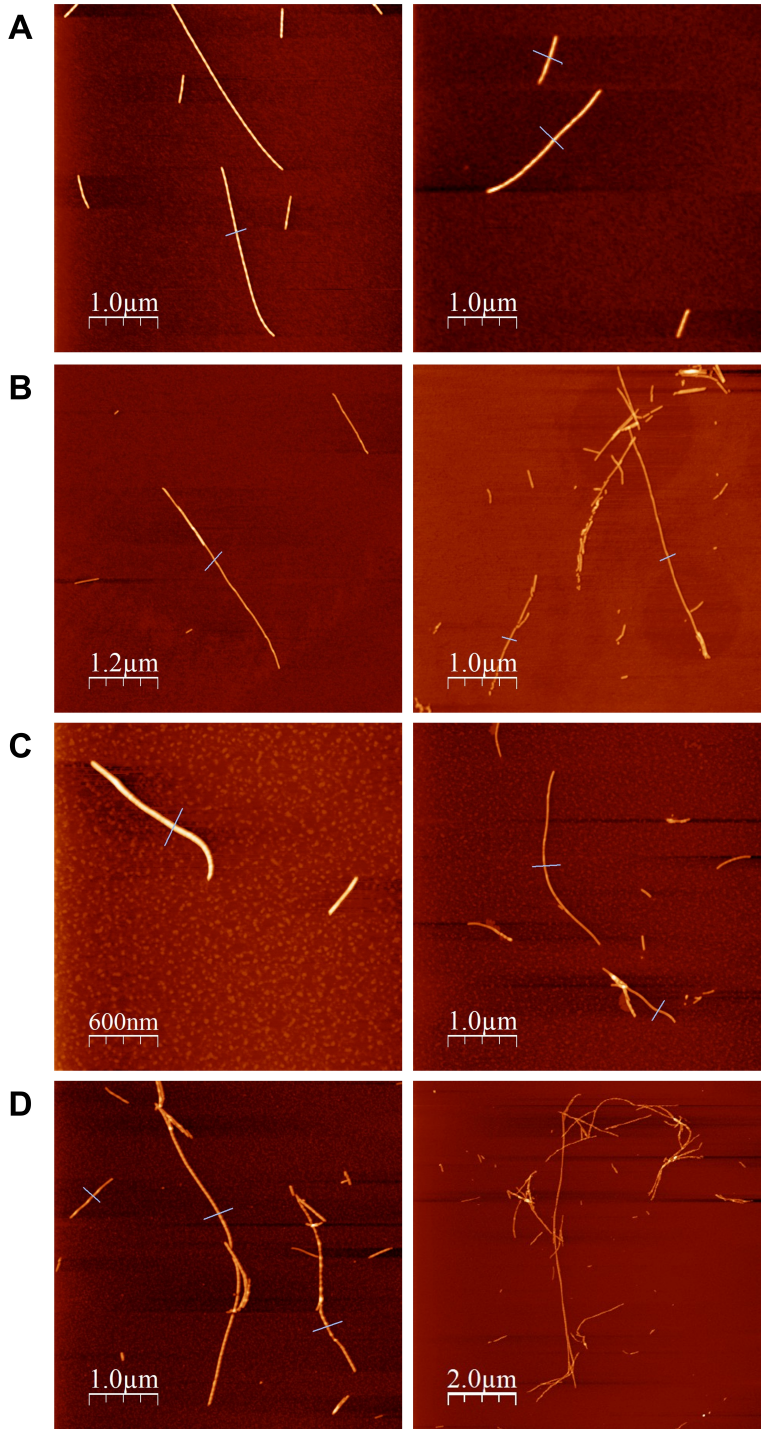

Figure 4.4: Atomic-force microscopy images of α-synuclein fibrils. Panels: (A) WT, (B) E46K, (C) H50Q, and (D) A53T; all prepared at a fibril concentration of 10 μM. Diameters were determined along the marked transects, and fibril periodicity was quantified in their immediate vicinity.

Parameter (nm)	WT	E46K	H50Q	A53T
Diameter	5.3, 4.8, 6.3	6.3, 5.8, 5.6	4.7, 4.2, 4.1	7.1, 6.8, 5.9
Average diameter	5.5 ± 0.8	5.90 ± 0.4	4.3 ± 0.3	6.6 ± 0.6
Periodicity	71.4, 70.6	63.4, 52.5	66.9, 62.1	75.2, 67.6
Average Periodicity	71.0 ± 0.6	58.0 ± 7.7	64.5 ± 3.4	71.4 ± 5.4

Table 4.1: Comparison of fibril diameter and periodicity for the four α-synuclein variants. All individual diameter and periodicity measurements are displayed, and the corresponding means are annotated with ±, SD error bars.

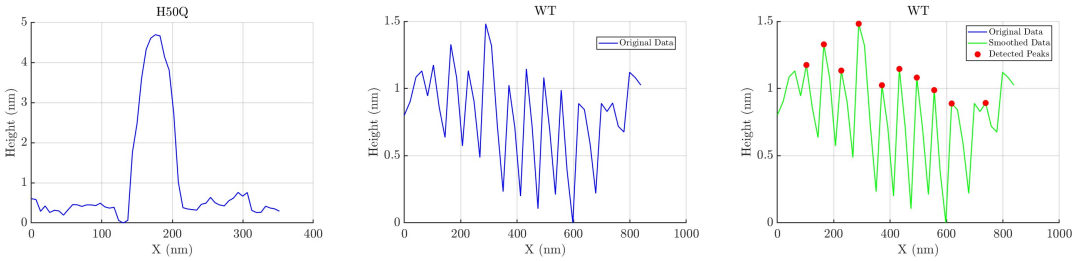

Figure 4.5: Example of fibril diameter and periodicity determination used in this work. The left graph displays the height profile across an H50Q fibril. The middle and right graphs represent samples from a WT fibril. The middle graph shows the height profile traced along the fibril's surface, while the right graph highlights the identified peaks using MATLAB's `findpeaks` function for periodicity calculations.

4.5 Esterase activity assay

A total of 13 esterase kinetic experiments were performed using a range of substrate concentrations, as summarized in Figure 4.6 and Table 4.2. Each variant's esterase activity was plotted as a function of substrate concentration, and the resulting MM curves showed an excellent fit to the model. Averaging across replicates, E46K showed the highest turnover capacity (14.9 ± 3.82) as seen in Table 4.2, while the mean of its MM constant is similar to WT (23.3 ± 14.6 mM vs. 22.2 ± 10.5 mM), indicating that E46K fibrils are more catalytically efficient. The mean V_{max} for H50Q fibrils resulted in 9.21 ± 2.00 µM which is comparable to WT fibrils, but with significantly lower K_m. The single A53T measurement yielded intermediate parameters.

All experiments were carried out independently, and each data point represents the average of three technical replicates. Since each variants was measured only few times (WT, E46K, H50Q n = 4; A53T n =1), the observed differences in V_{max} and K_m are tentative and require additional experiments for confirmation.

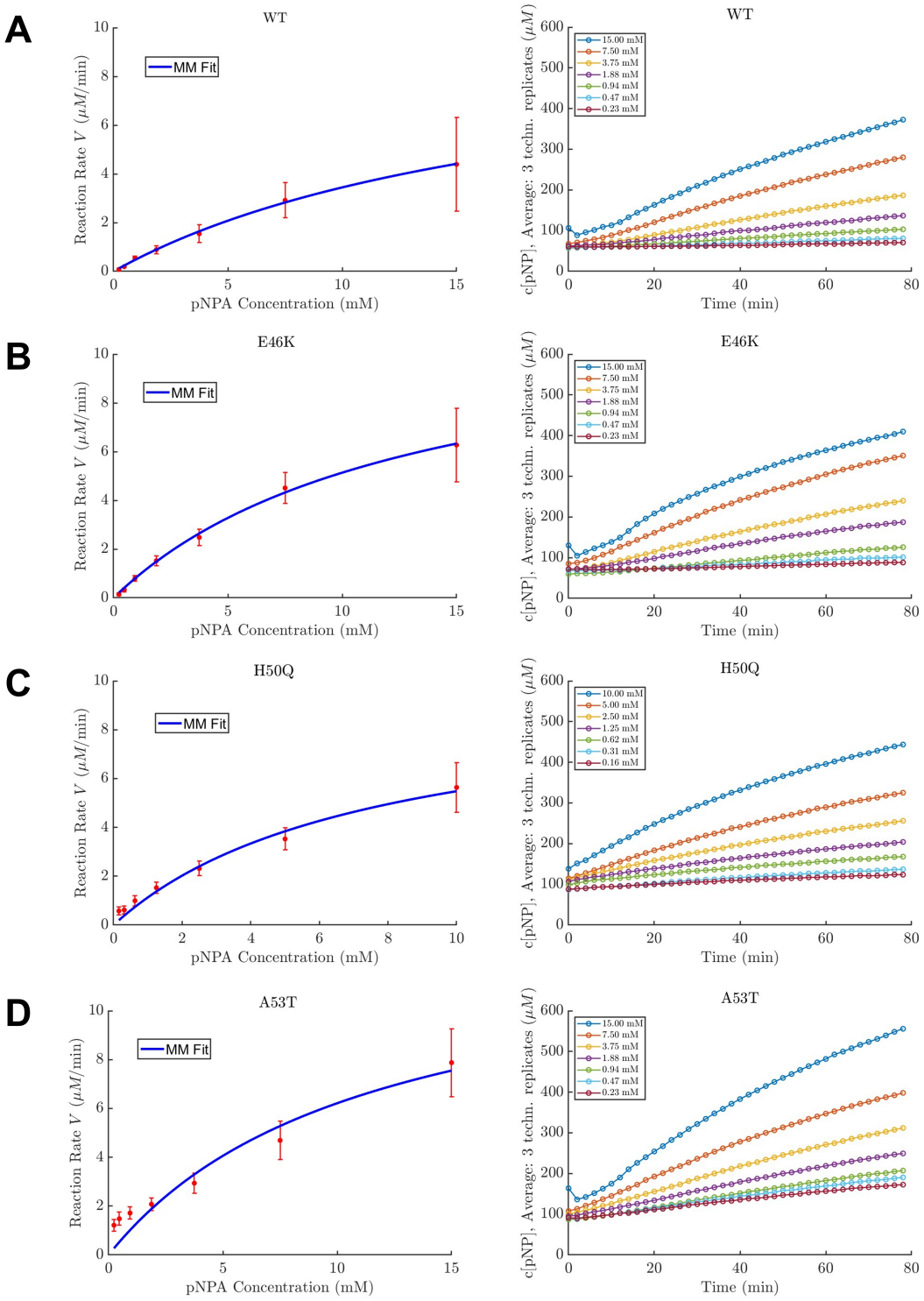

Figure 4.6: Esterase activity of four aSyn variants. Each horizontal panel represents one variant: Panel A: WT, Panel B: E46K, Panel C: H50Q, and Panel D: A53T. Each assay was performed with 20 µM amyloid fibrils, while the pNPA substrate concentration ranged from 10-15 mM. Graphs on the left represent Michaelis-Menten curves, while graphs on the right represent the concentration of the cleaved substrate (background subtracted). Error bars visualize the SD of the technical replicates within single experiment. Initial rates for MM curves were obtained by linear regression of product concentration vs. time over the 4-20 min interval.

Parameter	WT	E46K	H50Q	A53T
V_{max}(µM/min)	5.29, 13.9, 10.1, 6.68	13.2, 11.8, 19.74, 11.7	9.58, 9.32, 8.74, 5.26	13.3
Average V_{max}(µM/min)	9.93 ± 3.84	14.9 ± 3.82	9.21 ± 2.00	13.3
K_m(mM)	13.1, 34.3, 19.2, 10.9	15.3, 13.0, 41.6, 9.61	7.48, 13.12, 12.6, 4.23	11.3
Average K_m(mM)	22.2 ± 10.5	23.3 ± 14.6	11.1 ± 4.26	11.3

Table 4.2: Michaelis–Menten kinetic parameters, V_{max} and K_m, from all individual experiments performed with varying pNPA concentrations and 20 µM aSyn amyloid fibrils. The table includes results from each individual experiment, along with the corresponding mean and SD for both V_{max} and K_m.

4.6 Phosphatase activity assay

Unlike in the esterase assay, the phosphatase activity was too weak to fit a Michaelis–Menten model. The results are displayed as absorbance values of the most active experiment as well as final concentrations of each individual experiment as seen in Figure 4.7. To enable direct comparison between fibrils and their respective controls (monomers or buffer background), the absorbance values were baselined to start from zero. Figure 4.7 indicates that WT and A53T exhibit considerably greater activity than E46K and H50Q (even with single active WT experiment), with E46K being essentially inactive, while H50Q retains measurable but lower activity.

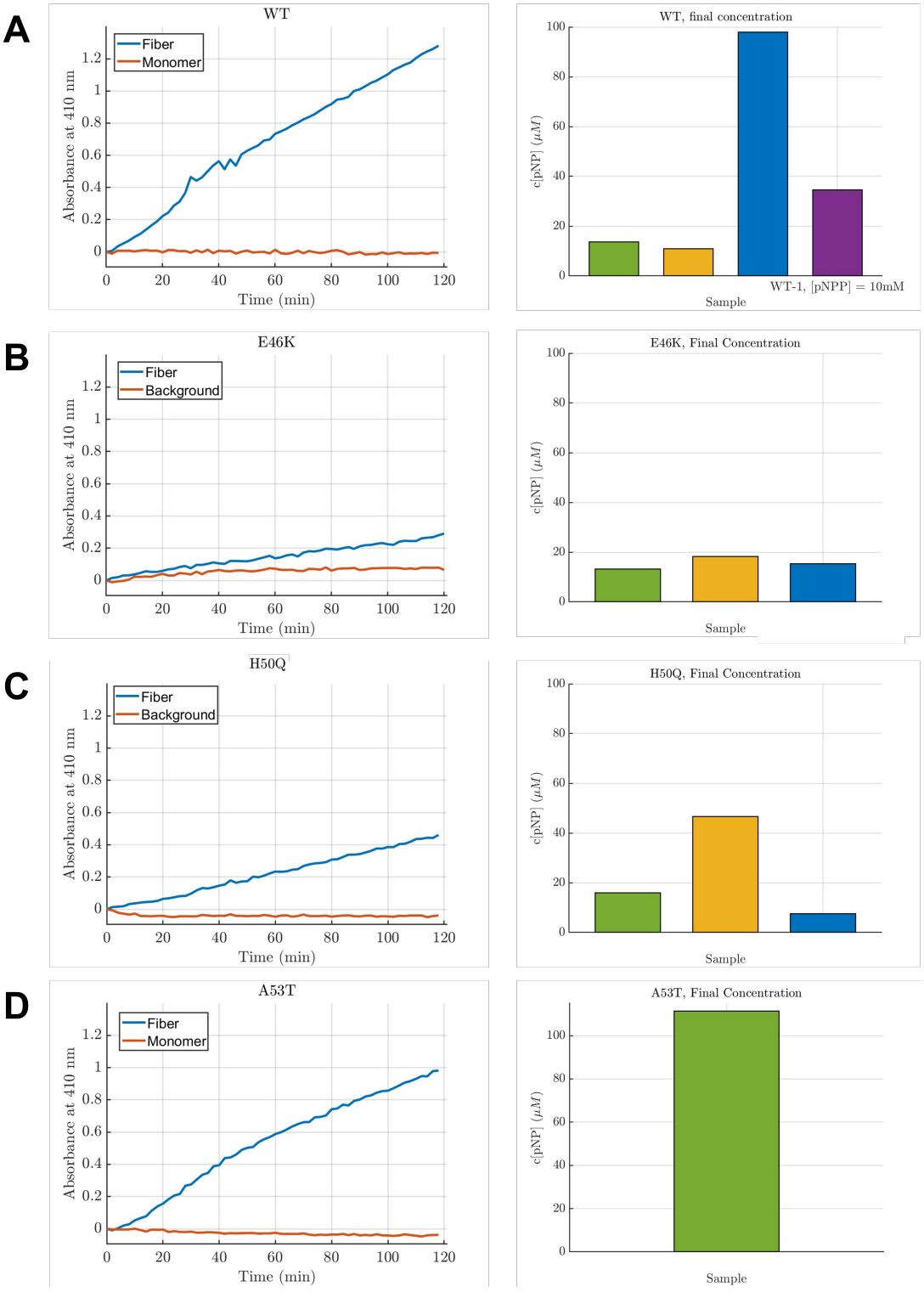

Figure 4.7: Phosphatase activity of four variants. Each horizontal panel represents one variant. Each assay was performed with 20 µM amyloid fibrils, while the pNPA substrate concentration ranged from 10-15 mM. Bar plots on right represent final concentration of product buildup of each individual experiment. The graphs on left correspond the absorbance values of the experiment with the highest final pNP concentration. Absorbance values of fibrils are compared with control group (background buffer or corresponding monomer).

4.7 ATPase activity assay

ATPase activity was measured at discrete time points, unlike previous assays, which were measured continuously. In Figure 4.8, H50Q and A53T fibrils show clearly higher ATPase activity than both the WT and E46K variants. The results, recorded as concentration values, were obtained by using 1 mM ATP as substrate. Measurements were taken at four time points; at 0 h, 1 h, 2 h, and 4 h, with an additional deadtime of 5-10 min. Fibril activity was compared to a control group comprising either monomers or buffer background. Echoing phosphatase activity, and in contrast to esterase activity, ATPase assay provided mixed results between the variants, suggesting that H50Q and A53T enhance ATPase functionality relative to the WT and E46K variants. One set of experiment was performed per variant.

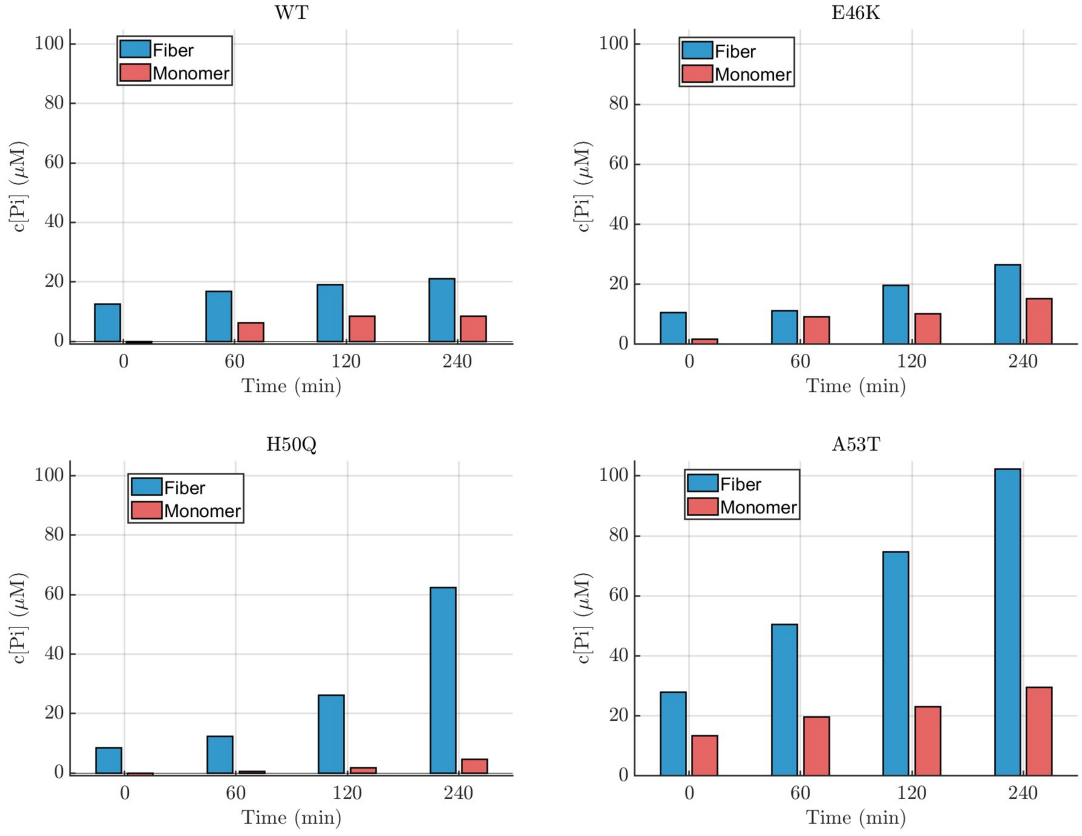

Figure 4.8: ATPase activity of four variants. Each assay was performed with 40 µM amyloid fibrils, while the ATP substrate concentration was 1 mM. Results display concentration values of product produced by the fibrils and a control group (background buffer or corresponding monomer). Measured time points are 0, 60, 120, 240 min.

5

Discussion and Conclusion

All variants of α-Synuclein fibrils prepared in this work showed significant esterase activity, supporting the notion that esterase-like catalytic sites are distributed across the fibril surface. Differences in esterase activity between the variants are not statistically significant due to measurement error being large relative to the small number of replicates. On other hand, dephosphorylation activities (phosphatase and ATPase) were far more heterogeneous, even within a same variant. Although A53T fibrils displayed the highest activity across all assays, this finding is uncertain due to lack of repetition of experiments. E46K had no significant activity in any both of the dephosphorylation assays, while WT and H50Q had varying levels of phosphatase and ATPase activity. Both WT and H50Q had one experiment where the fibrils were extremely active in dephosphorylation.

In vitro, aSyn forms a few well characterized fibril polymorphs. Depending how β-arch kernels attach on each other, polymorphs may vary with the influence of buffer and pH used. Cryo-em shows two buffer-selective WT polymorph folds, tetrabutylphosphoniuum bromide grown fold-1 (rod and twister) and Tris/KCL-grown fold-2 (2a and 2b) [42], [43]. For pathogenic mutations (E46k, H50QQ and A53T) point mutations reshape these kernels. H50Q fibrils retain the WT rod-like β-arch core, but replacing His50 removes the H50-E57 interaction and shifts the protofilament pairing [44]. E46K removes the E46-K80 salt bridge and repacks the protofilament fold into stabler fibril [21]. A53T substitution removes 50-57 steric zipper, shrinking the buried protofilament causing looser fibrils structure [45]. The aSyn fibrils grown in this thesis varied in buffers but pH was kept close to physiologically neutral pH.

Previous reports have attributed phosphatase activity to WT aSyn fibrils, but results in this work suggest that this activity is not an inherent property of the WT sequence. Subtle differences in experimental conditions might affect the results such as buffer composition, ionic strength, pH, fibril maturation and storing time etc. These changes might contribute to whether the catalytic pocket for phosphatase activity is available or not. The fact that most variants retained at least some phosphatase function (with E46K being the exception) further supports a hypothesis in which only a handful of surface-exposed sites are truly competent for dephosphorylation. Mutations or small structural differences in fibril formation might alter those key residues or backbone conformations and therefore abolish this activity. To draw firmer conclusions, the phosphatase and ATPase assays should be repeated with varying conditions in order to produce reproducible data. A systematic titration of solution variables, such as pH, salt concentration, the presence of co-factor, would

help to define the precise conditions under which aSyn fibrils become catalytically active as phosphatases. In addition, it would be important to test the activity of fibrils seeded with patient-derived material, as these are likely to adopt structural features more closely resembling in vivo fibrils.

If aSyn fibrils can act as esterases, phosphatases and ATPases inside the neurons, they could reshape local metabolite levels. An uncontrolled increase of ATP hydrolysis at aSyn fibril surface would further reduce the ATP content in dopaminergic neurons where ATP production has been reported to be decreased [13]. Although the ATPase activity of aSyn fibrils is much lower compared to typical ATPase enzymes, the large amount of fibrils present could make this activity significant, leading to a local drop in ATP levels. Reduced levels of ATP have also been reported in vivo studies of PD patients in the midbrain, basal ganglia and occipital lobe [46], which could potentially be explained by the catalytic activity of aSyn fibrils. Because these fibrils can catalyze model esters, phosphomonoesters and ATP under assay (near-physiological) buffers, they may directly affect neuronal energy and signaling metabolism, aligning with metabolic hallmarks of Parkinson's disease.

References

[1] Parkinson's Foundation, *Statistics | Parkinson's Foundation*, https://www.parkinson.org/understanding-parkinsons/statistics, Online; accessed 29 April 2025, 2025.

[2] D. Eisenberg and M. Jucker, "The amyloid state of proteins in human diseases," *Cell*, vol. 148, no. 6, pp. 1188–1203, 2012.

[3] J. D. Flynn, R. P. McGlinchey, R. L. Walker, and J. C. Lee, "Structural features of α-synuclein amyloid fibrils revealed by raman spectroscopy," *Journal of Biological Chemistry*, vol. 293, no. 3, pp. 767–776, 2018.

[4] S. Mantri and J. F. Morley, "Prodromal and early parkinson's disease diagnosis," *Pract Neurol*, vol. 35, pp. 28–31, 2018.

[5] P. Wittung-Stafshede, "Chemical catalysis by biological amyloids," *Biochemical Society Transactions*, vol. 51, no. 5, pp. 1967–1974, 2023.

[6] I. Horvath and P. Wittung-Stafshede, "Amyloid fibers of α-synuclein catalyze chemical reactions," *ACS Chemical Neuroscience*, vol. 14, no. 4, pp. 603–608, 2023.

[7] I. Horvath, K. A. Mohamed, R. Kumar, and P. Wittung-Stafshede, "Amyloids of α-synuclein promote chemical transformations of neuronal cell metabolites," *International Journal of Molecular Sciences*, vol. 24, no. 16, p. 12 849, 2023.

[8] L. V. Kalia and A. E. Lang, "Parkinson's disease," *The lancet*, vol. 386, no. 9996, pp. 896–912, 2015.

[9] Parkinson Society British Columbia, *About parkinson's*, https://parkinson.bc.ca/resources-support/about-parkinsons, Accessed 29 April 2025, 2025.

[10] T. Lancet, *What next in parkinson's disease?* 2024.

[11] L. Breydo, J. W. Wu, and V. N. Uversky, "α-synuclein misfolding and parkinson's disease," *Biochimica et Biophysica Acta (BBA)-Molecular Basis of Disease*, vol. 1822, no. 2, pp. 261–285, 2012.

[12] National Institute of Neurological Disorders and Stroke. "Parkinson's disease." National Institutes of Health, U.S. Department of Health and Human Services. (2025), [Online]. Available: https://www.ninds.nih.gov/health-information/disorders/parkinsons-disease (visited on 06/16/2025).

[13] A. Bose and M. F. Beal, "Mitochondrial dysfunction in parkinson's disease," *Journal of neurochemistry*, vol. 139, pp. 216–231, 2016.

[14] V. Dias, E. Junn, and M. M. Mouradian, "The role of oxidative stress in parkinson's disease," *Journal of Parkinson's disease*, vol. 3, no. 4, pp. 461–491, 2013.

[15] Z.-X. Wang, Y.-L. Li, J.-L. Pu, and B.-R. Zhang, "Dna damage-mediated neurotoxicity in parkinson's disease," *International Journal of Molecular Sciences*, vol. 24, no. 7, p. 6313, 2023.

[16] L. Chen, Q. Shen, Y. Liu, *et al.*, "Homeostasis and metabolism of iron and other metal ions in neurodegenerative diseases," *Signal Transduction and Targeted Therapy*, vol. 10, no. 1, p. 31, 2025.

[17] StressMarq Biosciences Inc., *Alpha-synuclein protein (spr-316)*, Accessed: 2025-05-05, n.d. [Online]. Available: `https://www.stressmarq.com/products/protein/alpha-synuclein-protein-spr-316/`.

[18] K. Rosborough, N. Patel, and L. V. Kalia, "α-synuclein and parkinsonism: Updates and future perspectives," *Current neurology and neuroscience reports*, vol. 17, pp. 1–11, 2017.

[19] Y. Li, C. Zhao, F. Luo, *et al.*, "Amyloid fibril structure of α-synuclein determined by cryo-electron microscopy," *Cell research*, vol. 28, no. 9, pp. 897–903, 2018.

[20] R. Guerrero-Ferreira, N. M. Taylor, D. Mona, *et al.*, "Cryo-em structure of alpha-synuclein fibrils," *elife*, vol. 7, e36402, 2018.

[21] D. R. Boyer, B. Li, C. Sun, *et al.*, "The α-synuclein hereditary mutation e46k unlocks a more stable, pathogenic fibril structure," *Proceedings of the National Academy of Sciences*, vol. 117, no. 7, pp. 3592–3602, 2020.

[22] M. Sawaya, *Amyloid Atlas*, Online: `https://people.mbi.ucla.edu/sawaya/amyloidatlas/`, Last updated April 16, 2025; accessed April 29, 2025, 2025.

[23] B. Fongaro, E. Cappelletto, A. Sosic, B. Spolaore, and P. Polverino de Laureto, "3, 4-dihydroxyphenylethanol and 3, 4-dihydroxyphenylacetic acid affect the aggregation process of e46k variant of α-synuclein at different extent: Insights into the interplay between protein dynamics and catechol effect," *Protein Science*, vol. 31, no. 7, e4356, 2022.

[24] F. Chiti and C. M. Dobson, "Protein misfolding, amyloid formation, and human disease: A summary of progress over the last decade," *Annual review of biochemistry*, vol. 86, no. 1, pp. 27–68, 2017.

[25] E. Duran-Meza and R. Diaz-Espinoza, "Catalytic amyloids as novel synthetic hydrolases," *International Journal of Molecular Sciences*, vol. 22, no. 17, p. 9166, 2021.

[26] M. A. Hanspal, C. M. Dobson, J. J. Yerbury, and J. R. Kumita, "The relevance of contact-independent cell-to-cell transfer of tdp-43 and sod1 in amyotrophic lateral sclerosis," *Biochimica et Biophysica Acta (BBA)-Molecular Basis of Disease*, vol. 1863, no. 11, pp. 2762–2771, 2017.

[27] G. Meisl, J. B. Kirkegaard, P. Arosio, *et al.*, "Molecular mechanisms of protein aggregation from global fitting of kinetic models," *Nature protocols*, vol. 11, no. 2, pp. 252–272, 2016.

[28] N. Vettore and A. K. Buell, "Thermodynamics of amyloid fibril formation from chemical depolymerization," *Physical Chemistry Chemical Physics*, vol. 21, no. 47, pp. 26 184–26 194, 2019.

[29] K. Wilson, A. Hofmann, J. M. Walker, and S. Clokie, *Wilson and Walker's principles and techniques of biochemistry and molecular biology*. Cambridge university press, 2018.

[30] K. Morgan. "Plasmids 101: Origin of replication." Accessed: 2025-04-18. (2020), [Online]. Available: https://blog.addgene.org/plasmid-101-origin-of-replication.

[31] T. F. Scientific, *Bacterial transformation workflow*, Accessed: 2025-04-23, 2025. [Online]. Available: https://www.thermofisher.com/fi/en/home/life-science/cloning/cloning-learning-center/invitrogen-school-of-molecular-biology/molecular-cloning/transformation/bacterial-transformation-workflow.html.

[32] E. Amann, J. Brosius, and M. Ptashne, "Vectors bearing a hybrid trp-lac promoter useful for regulated expression of cloned genes in escherichia coli," *Gene*, vol. 25, no. 2-3, pp. 167–178, 1983.

[33] T. F. S. Inc., *Novex sharp pre-stained protein standard protocol*, Publication No. MAN0005693 Rev C.0, Thermo Fisher Scientific, Life Technologies Corporation, 2014. [Online]. Available: https://www.lifetechnologies.com/support.

[34] S. A. Hudson, H. Ecroyd, T. W. Kee, and J. A. Carver, "The thioflavin t fluorescence assay for amyloid fibril detection can be biased by the presence of exogenous compounds," *The FEBS journal*, vol. 276, no. 20, pp. 5960–5972, 2009.

[35] C. Xue, T. Y. Lin, D. Chang, and Z. Guo, "Thioflavin t as an amyloid dye: Fibril quantification, optimal concentration and effect on aggregation," *Royal Society open science*, vol. 4, no. 1, p. 160 696, 2017.

[36] S. M. Kelly, T. J. Jess, and N. C. Price, "How to study proteins by circular dichroism," *Biochimica et Biophysica Acta (BBA)-Proteins and Proteomics*, vol. 1751, no. 2, pp. 119–139, 2005.

[37] Y. Wei, A. A. Thyparambil, and R. A. Latour, "Protein helical structure determination using cd spectroscopy for solutions with strong background absorbance from 190 to 230 nm," *Biochimica et Biophysica Acta (BBA)-Proteins and Proteomics*, vol. 1844, no. 12, pp. 2331–2337, 2014.

[38] LibreTexts, *Circular Dichroism*, Accessed: 2025-03-20, 2025. [Online]. Available: https://chem.libretexts.org/Bookshelves/Physical_and_Theoretical_Chemistry_Textbook_Maps/Supplemental_Modules_%28Physical_and_Theoretical_Chemistry%29/Spectroscopy/Electronic_Spectroscopy/Circular_Dichroism.

[39] Y. An, S. S. Manuguri, and J. Malmström, "Atomic force microscopy of proteins," *Protein Nanotechnology: Protocols, Instrumentation, and Applications*, pp. 247–285, 2020.

[40] B. Srinivasan, "A guide to the michaelis–menten equation: Steady state and beyond," *The FEBS journal*, vol. 289, no. 20, pp. 6086–6098, 2022.

[41] I. Horcas, R. Fernandez, J. M. Gomez-Rodriguez, J. Colchero, J. Gomez-Herrero, and A. M. Baro, "Wsxm: A software for scanning probe microscopy and a tool for nanotechnology," *Review of Scientific Instruments*, vol. 78, no. 1, p. 013 705, 2007. DOI: 10.1063/1.2432410.

[42] R. Guerrero-Ferreira, N. M. Taylor, A.-A. Arteni, *et al.*, "Two new polymorphic structures of human full-length alpha-synuclein fibrils solved by cryo-electron microscopy," *Elife*, vol. 8, e48907, 2019.

[43] B. Li, P. Ge, K. A. Murray, *et al.*, "Cryo-em of full-length α-synuclein reveals fibril polymorphs with a common structural kernel," *Nature communications*, vol. 9, no. 1, p. 3609, 2018.

[44] D. R. Boyer, B. Li, C. Sun, *et al.*, "Structures of fibrils formed by α-synuclein hereditary disease mutant h50q reveal new polymorphs," *Nature structural & molecular biology*, vol. 26, no. 11, pp. 1044–1052, 2019.

[45] Y. Sun, S. Hou, K. Zhao, *et al.*, "Cryo-em structure of full-length α-synuclein amyloid fibril with parkinson's disease familial a53t mutation," *Cell research*, vol. 30, no. 4, pp. 360–362, 2020.

[46] Y. Jing, A. Haeger, F. Boumezbeur, F. Binkofski, K. Reetz, and S. Romanzetti, "Neuroenergetic alterations in neurodegenerative diseases: A systematic review and meta-analysis of in vivo 31p-mrs studies," *Ageing Research Reviews*, p. 102 488, 2024.

A

Appendix 1

This section contains complementary data on esterase activity, including visualizations for the WT, E46K and H50Q α-Synuclein variants. In addition, Michaelis-Menten curves from ATPase activity assays are presented for variants where the data followed the expected curve shape, despite large fitting errors: WT and H50Q. This contrasts with E46K that produced non-interpretable curve.

A.1 Esterase Activity Assay results

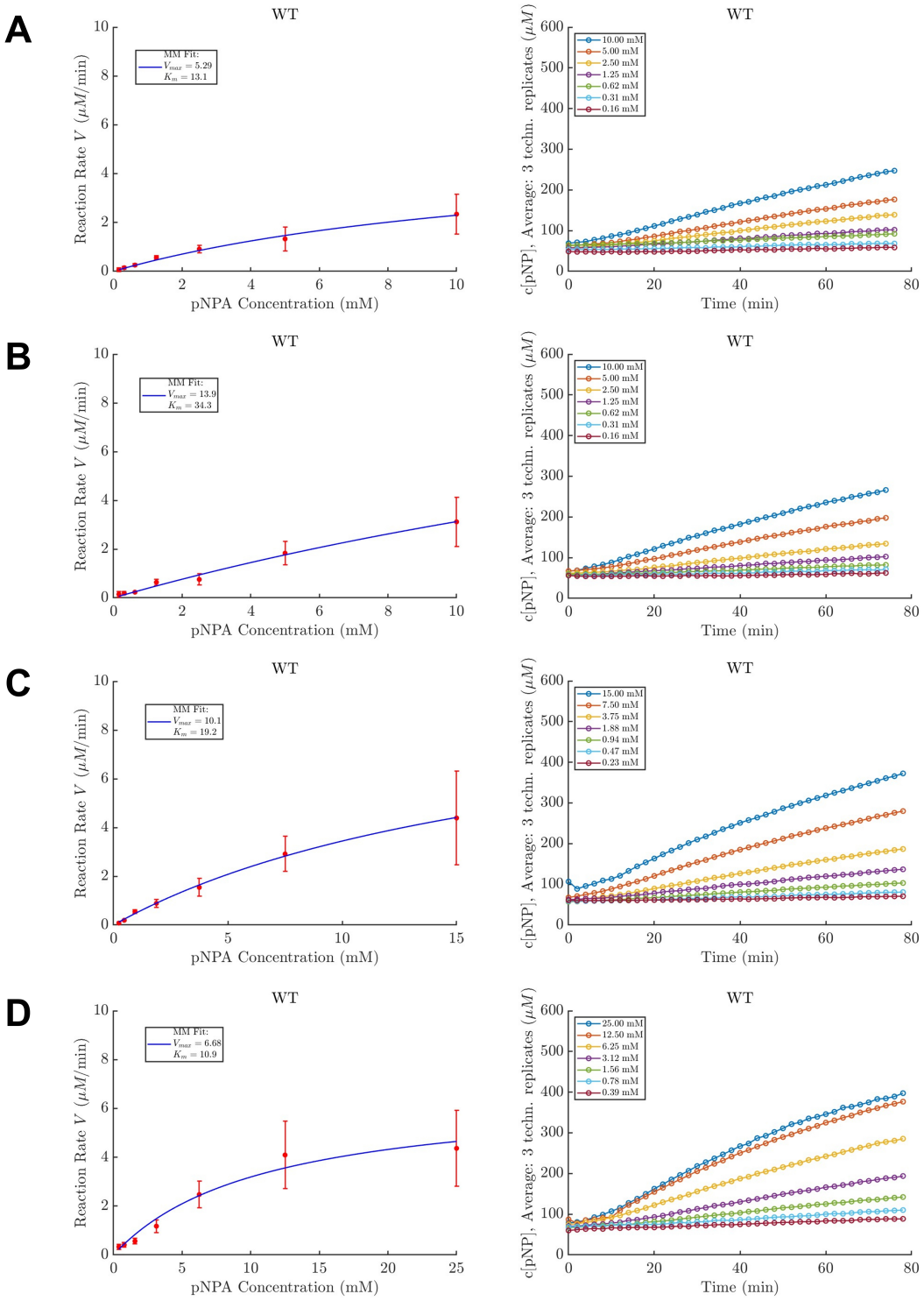

Figure A.1: Esterase activity of aSyn WT. Each row represent one individual experiment with 3 technical replicates.

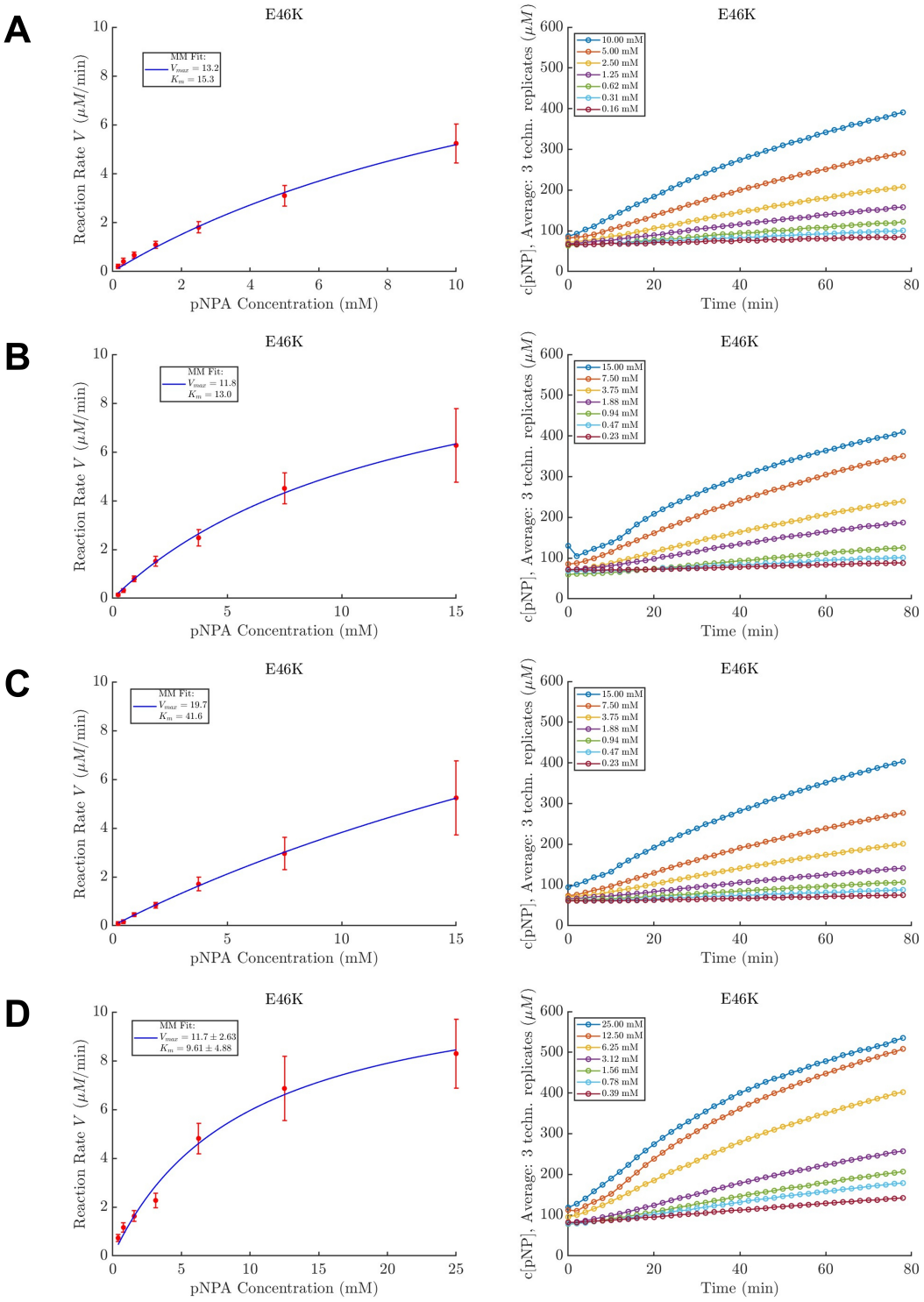

Figure A.2: Esterase activity of aSyn E46K. Each row represent one individual experiment with 3 technical replicates.

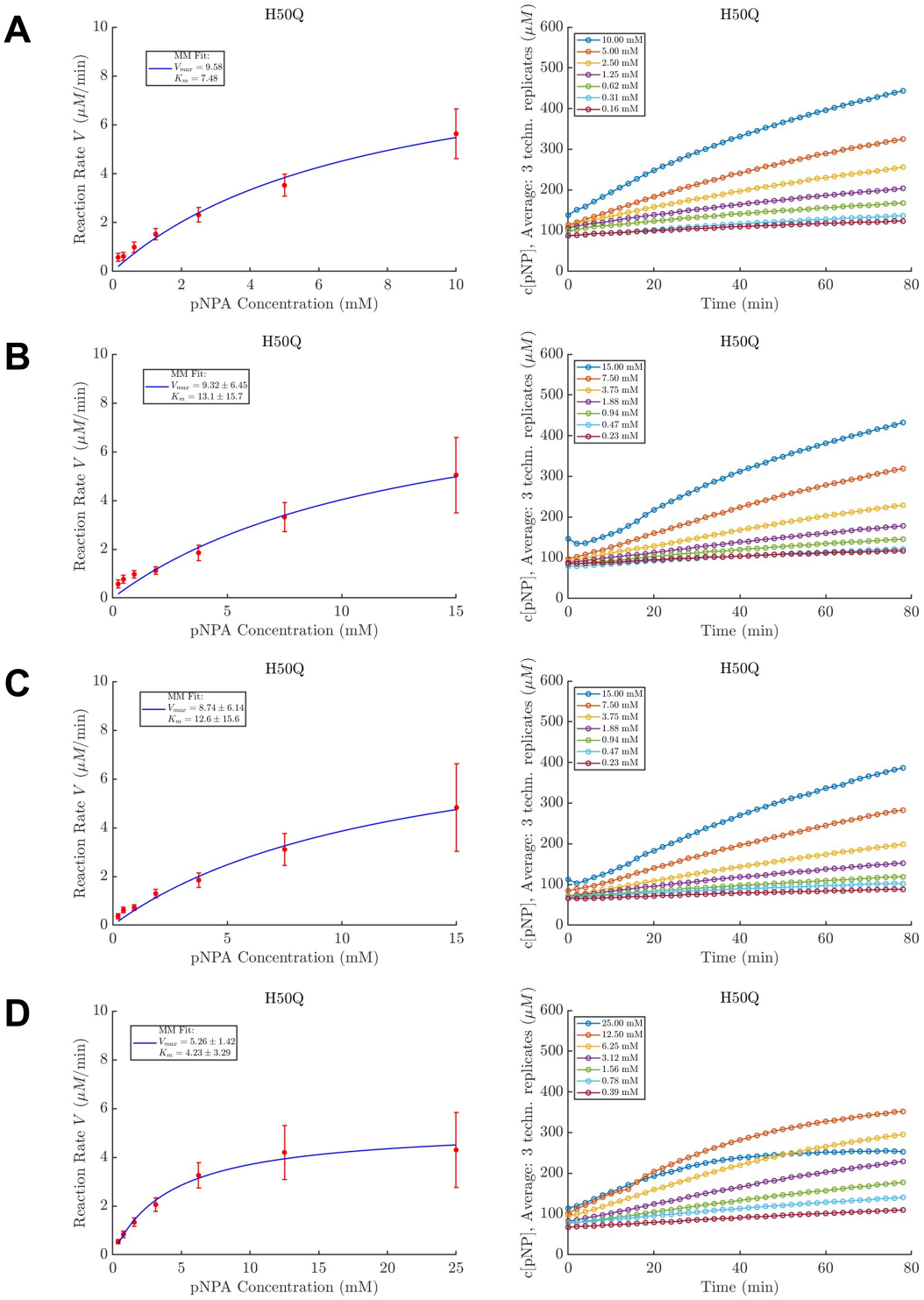

Figure A.3: Esterase activity of aSyn H50Q. Each row represent one individual experiment with 3 technical replicates.

A.2 ATPase Activity Assay results

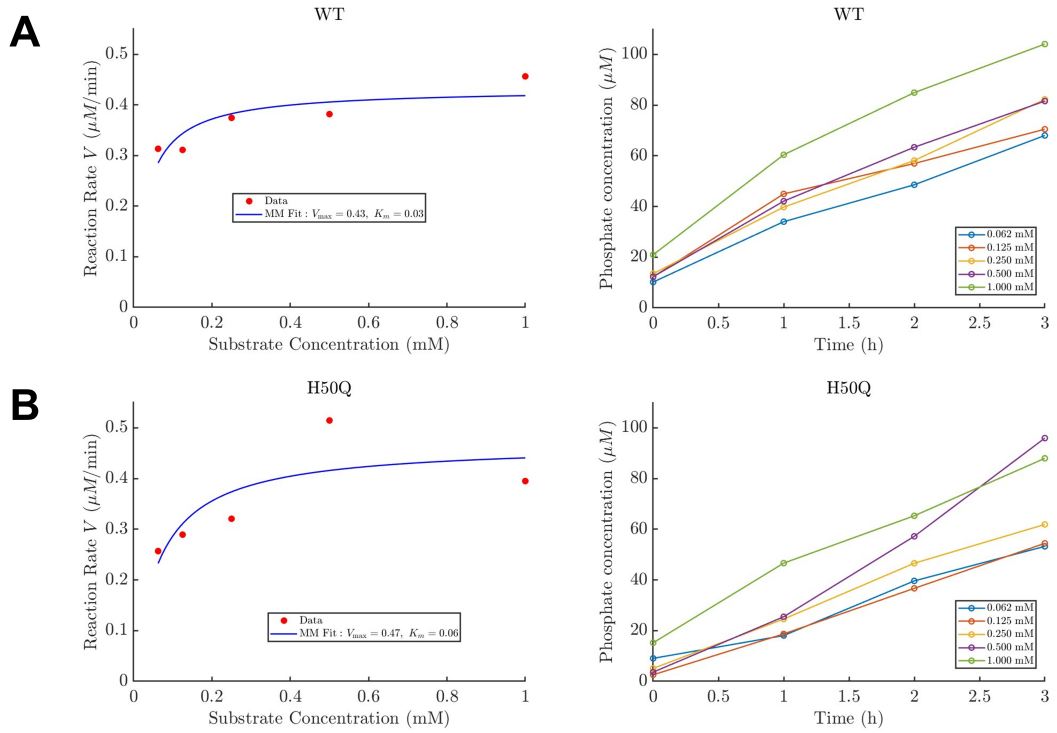

Figure A.4: ATPase vivacity of aSyn WT and H50Q. Row A shows results for WT and row B for H50Q. The left panel displays MM curves based on five substrate concentrations. The right panel shows the corresponding phosphate concentrations used to calculate the initial reaction rates.

DEPARTMENT OF SOME SUBJECT OR TECHNOLOGY
CHALMERS UNIVERSITY OF TECHNOLOGY
Gothenburg, Sweden
www.chalmers.se

CHALMERS
UNIVERSITY OF TECHNOLOGY